

ON THE NATURE OF THE LOCAL SPIRAL ARM OF THE MILKY WAY

Y. Xu¹, J. J. Li^{1,2}, M. J. Reid³, K. M. Menten², X. W. Zheng⁴, A. Brunthaler², L. Moscadelli⁵, T. M. Dame³ and B. Zhang²

ABSTRACT

Trigonometric parallax measurements of nine water masers associated with the Local arm of the Milky Way were carried out as part of the BeSSeL Survey using the VLBA. When combined with 21 other parallax measurements from the literature, the data allow us to study the distribution and 3-dimensional motions of star forming regions in the spiral arm over the entire northern sky. Our results suggest that the Local arm does not have the large pitch angle characteristic of a short spur. Instead its active star formation, overall length (> 5 kpc), and shallow pitch angle ($\sim 10^\circ$) suggest that it is more like the adjacent Perseus and Sagittarius arms; perhaps it is a branch of one of these arms. Contrary to previous results, we find the Local arm to be closer to the Perseus than to the Sagittarius arm, suggesting that a branching from the former may be more likely. An average peculiar motion of near-zero toward both the Galactic center and north Galactic pole, and counter rotation of ~ 5 km s⁻¹ were observed, indicating that the Local arm has similar kinematic properties as found for other major spiral arms.

Subject headings: masers – techniques: high angular resolution – astrometry – stars: formation – galaxy: spiral arm – galaxy: kinematics and dynamics

¹Purple Mountain Observatory, Chinese Academy of Sciences, Nanjing 210008, China; xuye@pmo.ac.cn

²Max-Planck-Institut für Radioastronomie, Auf dem Hügel 69, 53121 Bonn, Germany

³Harvard-Smithsonian Center for Astrophysics, 60 Garden Street, Cambridge, MA 02138, USA

⁴Nanjing University, Nanjing 20093, China

⁵INAF-Osservatorio Astrofisico di Arcetri, Largo E. Fermi 5, 50125 Firenze, Italy

1. INTRODUCTION

Determining the spiral structure of our Milky Way has been a long-standing problem in astrophysics, since pioneering studies by Morgan et al. (1952, 1953) revealed three spiral arm segments in the solar neighborhood by spectroscopic parallax. However, progress has been hampered by the difficulty in identifying spectroscopic distances for distant sources, because of large and variable extinction from interstellar dust in the galactic plane. Although distances derived with other methods, such as kinematic distances, offer opportunities for progress, as demonstrated by Georgelin & Georgelin (1976) (GG76 hereafter) and Russeil et al. (2007), typical uncertainties are comparable to the spacing between arms and preclude identification of spiral arms of the Milky Way with confidence. At present, there is no general agreement on the number of arms nor on their locations and orientations. Churchwell et al. (2009) favor two arms from their investigation of counts of older stars, while observations of gas and dust indicate four- or five-arm models (Russeil 2003; Hou et al. 2009). Many dozens of models have been proposed (see the review of Liszt (1985); Steiman-Cameron (2010)), most of which are four-armed structures similar to that of GG76.

The major spiral arms within a few kpc of the Sun (Sagittarius and the Perseus arms) are well known, appearing as arcs in longitude-velocity plots of HI and CO emission (Oort et al. 1958; Bok 1959; Georgelin & Georgelin 1976; Dame et al. 2001). Parallaxes for high-mass star-forming regions (HMSFRs) now clearly locate the Sagittarius and the Perseus arms in the Galaxy with 3-dimensional positions and velocities (Choi, in preparation; Wu, in preparation). However, star-forming regions between these arms are known and collectively they have been called the “Orion spur”, the “Orion arm”, or the “Local arm” (Bok et al. 1970; Kerr 1970; Georgelin & Georgelin 1976; Avedisova 1985). Generally the Local arm was thought to be a secondary spiral feature, because the density of star-forming regions was significantly less than that of other major arms.

As part of the Bar and Spiral Structure Legacy (BeSSeL) Survey, we have been measuring trigonometric parallaxes for large numbers of HMSFRs. Somewhat surprisingly, we are also finding many sources thought to be in the Perseus arm (from kinematic distances) are instead associated with the Local arm. For example, we found that the HMSFR G075.76+00.33, which has a kinematic distance of ≈ 5.7 kpc and would locate it in the Perseus arm, has a distance measured by trigonometric parallax of 3.5 ± 0.3 kpc, which places it in the Local arm (Section 3). Based on BeSSeL Survey, VLBI Exploration of Radio Astrometry (VERA), and European VLBI Network (EVN) parallaxes, we can now identify 30 sources that are associated with the Local arm. Using these accurate distances and proper motions, we can now study the geometry and kinematics of the Local arm with unprecedented detail.

2. OBSERVATIONS

Observations of 22-GHz H₂O masers towards star-forming regions were carried out with the National Radio Astronomy Observatory (NRAO)¹ Very Long Baseline Array (VLBA), under programs BR145 and BM272. All sources were observed over 7- or 9-h tracks for projects BR145 or BM272, respectively. Table 1 lists details for the epochs observed. The observations consisted of three (BM272) or four (BR145) geodetic blocks, with phase-referenced observations inserted between these blocks. Details of the observational setup and calibration procedures can be found in Reid et al. (2009a). All data were processed on the DiFX² correlator in Socorro, NM (Deller et al. 2007).

For each maser source, we used several different background sources, selected from the VCS2 and VCS3 catalogs (Fomalont et al. 2003; Petrov et al. 2005) and our VLBI calibrator surveys (Xu et al. 2006a; Immer et al. 2011). H₂O masers can be time-variable with lifetimes of months to years. By comparison background compact extragalactic radio sources are relatively stable, so we used them as phase references when they were strong enough to do so. After making maps of both maser and background sources for all epochs, we measured the source positions and brightnesses by fitting elliptical Gaussian brightness distributions. Table 2 presents position and intensity data for the masers used for parallax measurements and the corresponding background sources, as well as other observational parameters. Absolute maser positions are derived from the positions of the corresponding VCS or ICRF sources (Ma et al. 1998), which are generally accurate within ≈ 1 mas.

¹The National Radio Astronomy Observatory is a facility of the US National Science Foundation operated under cooperative agreement with Associated Universities, Inc.

²This work made use of the Swinburne University of Technology software correlator, developed as part of the Australian Major National Research Facilities Programme and operated under licence.

Table 1. Details of the Epochs Observed

| Code | Source | Epoch 1 | Epoch 2 | Epoch 3 | Epoch 4 | Epoch 5 | Epoch 6 | Epoch 7 |
|--------|---------------|-------------|-------------|-------------|-------------|-------------|-------------|-------------|
| BM272 | ON 1 | 2008 Nov 11 | 2009 May 7 | 2009 Nov 14 | 2009 Dec 20 | 2010 May 5 | 2011 Feb 26 | ... |
| | G075.78+00.34 | ... | 2009 May 7 | ... | 2009 Dec 20 | 2010 May 5 | 2011 Feb 26 | ... |
| BR145D | G074.03–01.71 | 2010 Apr 24 | 2010 Jul 26 | 2010 Sep 25 | 2010 Nov 18 | 2010 Dec 16 | 2011 Apr 25 | ... |
| | G075.76+00.33 | 2010 Apr 24 | 2010 Jul 26 | 2010 Sep 25 | 2010 Nov 18 | 2010 Dec 16 | 2011 Apr 25 | ... |
| | G076.38–00.61 | 2010 Apr 24 | 2010 Jul 26 | 2010 Sep 25 | 2010 Nov 18 | 2010 Dec 16 | 2011 Apr 25 | ... |
| BR145E | G090.21+02.32 | 2010 May 16 | 2010 Aug 9 | 2010 Oct 12 | 2010 Nov 27 | 2010 Dec 31 | 2011 May 13 | ... |
| | G092.67+03.07 | 2010 May 16 | 2010 Aug 9 | 2010 Oct 12 | 2010 Nov 27 | 2010 Dec 31 | 2011 May 13 | ... |
| BR145S | G079.87+01.17 | 2011 May 24 | 2011 Aug 8 | 2011 Oct 30 | 2011 Nov 26 | 2012 Jan 12 | 2012 May 14 | 2012 Jun 29 |
| | G105.41+09.87 | 2011 May 24 | 2011 Aug 8 | 2011 Oct 30 | 2011 Nov 26 | 2012 Jan 12 | 2012 May 14 | 2012 Jun 29 |

3. RESULTS

Here we focus on parallax and absolute proper motion measurements; images of maser spots, background extragalactic continuum sources and internal maser motions are presented in the Online Material. Parallax and proper motion were fitted simultaneously to the data. Because systematic errors (owing to small uncompensated atmospheric delays and, in some cases, varying maser and calibrator source structures) typically dominate over thermal noise when measuring relative source positions, we added “error floors” in quadrature to the formal position uncertainties. We used different error floors for the Right Ascension and Declination data and adjusted them to yield post-fit residuals with χ^2 per degree of freedom near unity for both coordinates.

Except for G090.21+02.32, we used extragalactic continuum sources as the phase reference for the H₂O maser sources. For G090.21+02.32 the maser was used as the phase reference, because the relevant three extragalactic continuum sources were too faint to use as phase references. The quoted parallax uncertainty is the formal fitting uncertainty, multiplied by \sqrt{N} (where N is the number of maser spots used in the parallax fit) to account for possible correlations among the position measurements for the maser spots. The fitting results are presented in Table 3. Figures 1 – 9 show positions for the maser spots (relative to the background sources) as a function of time and the parallax fits.

H₂O masers can move fast (typically tens, but sometimes over 100 km s⁻¹) and spots are not always distributed uniformly around the exciting star. This can limit the accuracy of the estimate of the proper motion of the central, exciting star, used to study 3-D motions about the Milky Way. For G076.38–00.61, which exhibits a distribution characteristic of a fast bipolar outflow, its motion was determined by averaging the values from the redshifted and blueshifted spots separately, and then averaging these two results. With an outflow speed near 60 km s⁻¹, modest asymmetries in the outflows could result in an uncertain average. So we assigned a proper motion uncertainty of 20 km s⁻¹, which at its measured distance corresponds to 3 mas yr⁻¹. For sources with few spots (G079.87+01.17, G090.21+02.32 and G105.41+09.87), the proper motion of reference spot was used. These sources have simple maser spectra which span ≈ 10 km s⁻¹ or less, suggestive of modest outflow speeds, and we inflated the formal proper motion uncertainties to account for an unknown motion of a single maser spot relative to the central star of 10 km s⁻¹ at the measured distance. For sources with a symmetric distribution of maser spots or more than three spots that have proper motions, the motion of the central star was determined by averaging the motion of all maser spots, such as for ON1, G074.03–01.71, G075.76+00.33, G075.78+00.34 and G092.67+03.07.

Table 2. Positions and Brightnesses

| Source | R.A. (J2000) (^h ^m ^s) | Dec. (J2000) ([°] ['] ^{''}) | ϕ ([°]) | Brightness (Jy/beam) | V_{LSR} (km s^{-1}) | Beam (mas, mas, deg) |
|---------------|--|---|----------------------------|-------------------------|--|-------------------------|
| ON 1 | 20 10 09.2036 | +31 31 36.090 | | 34.1 | +14.8 | 0.9×0.4 @ –13 |
| J2003+3034 | 20 03 30.244061 | +30 34 30.78878 | 1.7 | 0.1 | | 0.9×0.4 @ –15 |
| G074.03–01.71 | 20 25 07.1053 | +34 49 57.593 | | 0.6 | +13.4 | 0.9×0.3 @ –13 |
| J2025+3343 | 20 25 10.842099 | +33 43 00.21448 | 1.1 | 3.9 | | 0.9×0.3 @ –14 |
| G075.76+00.33 | 20 21 41.0862 | +37 25 29.276 | | 5.3 | –9.6 | 0.8×0.3 @ –14 |
| J2015+3710 | 20 15 28.729794 | +37 10 59.51475 | 1.3 | 1.7 | | 0.9×0.3 @ –16 |
| G075.78+00.34 | 20 21 44.0097 | +37 26 37.446 | | 58.8 | +3.4 | 0.7×0.4 @ –13 |
| J2015+3710 | 20 15 28.729794 | +37 10 59.51475 | 1.3 | 2.3 | | 0.6×0.4 @ –15 |
| G076.38–00.61 | 20 27 25.4816 | +37 22 48.482 | | 0.2 | +6.9 | 0.8×0.3 @ –20 |
| J2015+3710 | 20 15 28.729794 | +37 10 59.51475 | 2.4 | 1.6 | | 0.8×0.3 @ –22 |
| G079.87+01.17 | 20 30 29.1464 | +41 15 53.590 | | 8.0 | –4.6 | 0.7×0.3 @ –19 |
| J2007+4029 | 20 07 44.9448 | +40 29 48.604 | 4.4 | 1.6 | | 0.7×0.3 @ –20 |
| G090.21+02.32 | 21 02 22.7007 | +50 03 08.309 | | 17.0 | –6.2 | 0.7×0.3 @ –9 |
| J2056+4940 | 20 56 42.73988 | +49 40 06.6011 | 1.0 | 0.03 | | 0.8×0.4 @ –10 |
| J2059+4851 | 20 59 57.87249 | +48 51 12.7002 | 1.3 | 0.05 | | 0.8×0.3 @ –9 |
| J2114+4953 | 21 14 15.03646 | +49 53 40.9552 | 1.9 | 0.06 | | 0.8×0.3 @ –8 |
| G092.67+03.07 | 21 09 21.7232 | +52 22 37.083 | | 26.1 | –3.7 | 0.7×0.3 @ –9 |
| J2117+5431 | 21 17 56.484452 | +54 31 32.50230 | 2.5 | 0.2 | | 0.8×0.4 @ –4 |
| G105.41+09.87 | 21 43 06.4628 | +66 06 55.183 | | 2.2 | –12.1 | 0.7×0.3 @ –10 |
| J2203+6750 | 22 03 12.62260 | +67 50 47.6730 | 2.6 | 0.2 | | 0.7×0.4 @ –6 |

Note. — ϕ is the angular separation between the maser and the calibrator. The absolute maser position, peak brightness, local standard of rest (LSR) velocity of the brightest spot, and a representative 2-dimensional size and position angle of the naturally weighted beam are listed for the first epochs for all sources except ON 1 (2009 May 7, the second epoch) and G105.41+09.87 (2011 October 30, the third epoch). Position angle is defined as east of north.

Table 3. Parallaxes & Proper Motions

| Maser Name | Π (mas) | D_{Π} (kpc) | μ_x (mas y ⁻¹) | μ_y (mas y ⁻¹) |
|---------------|----------------|--|-----------------------------------|-----------------------------------|
| ON 1 | 0.425±0.036 | 2.35 ^{+0.22} _{-0.18} | -3.22±0.05 | -5.54±0.06 |
| G074.03-01.71 | 0.629±0.017 | 1.59 ^{+0.04} _{-0.04} | -3.79±0.18 | -4.88±0.25 |
| G075.76+00.33 | 0.285±0.022 | 3.51 ^{+0.29} _{-0.25} | -3.08±0.06 | -4.56±0.08 |
| G075.78+00.34 | 0.281±0.034 | 3.56 ^{+0.49} _{-0.38} | -2.79±0.07 | -4.72±0.07 |
| G076.38-00.61 | 0.770±0.053 | 1.30 ^{+0.10} _{-0.08} | -3.73±3.00 | -3.84±3.00 |
| G079.87+01.17 | 0.620±0.027 | 1.61 ^{+0.07} _{-0.07} | -3.23±1.31 | -5.19±1.31 |
| G090.21+02.32 | 1.483±0.038 | 0.67 ^{+0.02} _{-0.02} | -0.67±3.13 | -0.90±3.13 |
| G092.67+03.07 | 0.613±0.020 | 1.63 ^{+0.06} _{-0.05} | -0.69±0.26 | -2.25±0.33 |
| G105.41+09.87 | 1.129±0.063 | 0.89 ^{+0.05} _{-0.05} | -0.21±2.38 | -5.49±2.38 |

Note. — Column 2 is the measured parallax. Column 3 is the parallax converted to distance. Columns 4 and 5 are proper motion in the eastward ($\mu_x = \mu_{\alpha} \cos \delta$) and northward directions ($\mu_y = \mu_{\delta}$), respectively.

3.1. Individual Sources

ON 1 is associated with IRAS 20081+3122, which coincides with an ultra-compact HII (UC HII) region (Kurtz et al. 2004). Yang et al. (2002) detected a high-velocity CO line wing, which was later confirmed as a bipolar outflow by both CO (Xu et al. 2006b) and H^{13}CO^+ lines (Kumar et al. 2004), indicating an active star-forming region. This source has measured parallaxes by Nagayama et al. (2011) with the VERA 22-GHz using H_2O masers and by Rygl et al. (2010) with the EVN using 6.7-GHz CH_3OH masers. We present our results in Table 3. Within the uncertainties all three measurements agree on the parallax, but there are slight differences among the proper motions. In order to calculate the peculiar motion of this source, we averaged the results of the three measurements (see Table 4).

G074.03–01.71, associated with IRAS 20231+3440, is located within Lynds 870. H_2O masers were first detected by Palla et al. (1993). Mao et al. (2002) detected a bipolar outflow from CO lines, which is likely to be driven by a low- or intermediate-mass young stellar object (YSO). This is further confirmed by its low IRAS luminosity ($500 L_\odot$ at a distance of 1.6 kpc, see Table 3) and non-detection of both CH_3OH and OH masers (van der Walt et al. 1996; Slysh et al. 1997), although it satisfies the criteria that Wood & Churchwell (1989a) used to identify embedded massive stars and UC HII regions.

G075.76+00.33 & **G075.78+00.34** (**ON 2N**) in **ON 2** are separated by $\approx 80''$ and associated with two different UC HII regions in the complex star-forming region ON 2 (Wood & Churchwell 1989b; Garay et al. 1993). H_2O masers in G075.78+00.34 are located $\sim 2''$ south of the peak of 6 cm radio continuum emission (Wood & Churchwell 1989b), which is spatially coincident with peaks of 7 mm continuum emission and NH_3 (3, 3) emission (Ando et al. 2011; Carral et al. 1997; Codella et al. 2010). The masers in G075.76+00.33, which are associated with IRAS 20198+3716, have an offset of $\approx 25''$ from the nearest detected UC HII region. The parallax and proper motion of G075.78+00.34 were also measured by Ando et al. (2011) with the VERA 22 GHz H_2O masers. Both measurements are consistent within the uncertainties, so the peculiar motion estimates are estimated by combining both results (see Table 4).

G076.38–00.61 is associated with IRAS 20255+3712 and Sharpless 106 (S 106) IR. This region has been widely studied at different wavelengths and angular resolutions (e.g., Kurtz et al. 1994; Smith et al. 2001; Schneider et al. 2002, 2007). Kurtz et al. (1994) found that the UC H II region G76.383–0.621 coincides with IRAS 20255+3712, which is offset $\approx 15''$ from the H_2O maser position. In the literature, the distance to G076.38–00.61 ranges from 0.5 to 5.7 kpc (Eiroa et al. 1979; Maucherat 1975). Although a distance of < 1 kpc is commonly used (e.g., Smith et al. 2001; Schneider et al. 2002), Schneider et al. (2007) suggested that S 106 is associated with the Cygnus X complex at about 1.7 kpc. This parallax distance

of $1.30_{-0.08}^{+0.10}$ kpc indicates that S 106 is close to the Cygnus X complex (parallax distance of 1.40 ± 0.08 kpc, Rygl et al. (2012)).

G079.87+01.17 is associated with IRAS 20286+4105 with an infrared luminosity of more than $5000 L_{\odot}$ at a distance of 1.6 kpc (see Table 3). It satisfies the IR criteria of Wood & Churchwell (1989a) for UC HII regions, although no radio centimeter-continuum emission is detected with the VLA (Molinari et al. 1998).

G090.21+02.32, associated with IRAS 21007+4951, is in the dark cloud Lynds 998. Its IRAS luminosity is $\sim 30 L_{\odot}$ at an assumed distance of 0.67 kpc (see Table 3), indicating a low-mass star-forming region, although it satisfies the criteria of Wood & Churchwell (1989a) for an UC HII region. This region has not been well studied to date. However, a CO bipolar outflow (Clark 1986) and SiO emission (Harju et al. 1998) indicate active star formation.

G092.67+03.07 is coincident with the submillimeter-continuum source JCMTSF J210921.7+522232 (Di et al. 2008). SiO emission has also been detected in this region (Harju et al. 1998). There are two IRAS sources, IRAS 21078+5211 and IRAS 21078+5209, with separations of $\approx 74''$ and $60''$, respectively. Both have infrared luminosity of $\sim 10^4 L_{\odot}$ at our measured distance of 1.63 kpc (see Table 3), indicating a HMSFR. However, G092.67+03.07 is not likely to be directly associated with either IRAS source given the large separations.

G105.41+09.87 is a deeply embedded YSO (Weintraub et al. 1994) associated with the LkH α 234 region in the NGC 7129 molecular cloud (Trinidad et al. 2004). The maser position coincides with the centimeter-continuum source VLA 3B, which is interpreted in terms of shock-induced ionization in a thermal radio jet rather than as an UC HII region (Trinidad et al. 2004). The parallax distance of $0.89_{-0.05}^{+0.05}$ kpc is consistent with a photometric distance of ~ 1 to 1.25 kpc (Racine 1968; Shevchenko & Yabukov 1989).

4. LOCATION AND PITCH ANGLE OF THE LOCAL ARM

Initial results from the BeSSeL Survey provide more than 60 sources with measured parallaxes. Many of these trace the Sagittarius arm inward from the Sun (Wu, in preparation) and the Perseus arm outward from the Sun (Choi, in preparation), clearly locating them in the Milky Way relative to the Sun. In addition, we find nine sources that are between Galactocentric distances of 7.8 and 8.7 kpc toward Galactic longitudes of $\sim 70^{\circ}$ or $\sim 105^{\circ}$. This places them between the Sagittarius arm and the Perseus arm. There are another 21 sources (including some low- and intermediate-mass star-forming regions) in the literature that also lie between the Sagittarius and Perseus arms (see Fig. 10). In a pair of accompanying papers (Choi, in preparation; Wu, in preparation) we find that the Sagittarius and Perseus arms

appear to be clear structures in longitude, velocity and distance. Here we define members of the Local arm as all sources that lie between these two structures, finding that they show a coherent pattern in space. Table 4 summarizes the parallax, proper motion, and v_{LSR} of these 30 sources.

The 30 star-forming regions in the Local arm trace a narrow, slightly curved, “swath” starting at ≈ 3.6 kpc toward $l \approx 60^\circ$ and extending ≈ 1.9 kpc toward $l \approx 230^\circ$ (Since there currently are no parallax distances measured between $l = 240^\circ$ and 270° , it is not clear how far the Local arm extends in the 3^{rd} Galactic quadrant.) Visually, the width of the swath is less than about 1 kpc, while the separation between the Sagittarius and Perseus arms in this region of the Galaxy is about 3.5 kpc. The Sun is located close to the inner edge of the arm.

Comparing the locations of the Sagittarius and Perseus arms, based on parallaxes (Choi, in preparation; Wu, in preparation), the distance between the centers of Local and Sagittarius arms is ≈ 2 kpc and between the Local and Perseus arms is ≈ 1.5 kpc (both measured along a line from the Galactic center through the Sun). Thus, contrary to previous claims (GG76, Vallée 2002), the Local arm is nearer to the Perseus than to the Sagittarius arm.

It has been suggested that the Local arm is an interarm branch or spur (GG76). Spurs and branches are often observed in external galaxies (Elmegreen 1980; Scoville et al. 2001; La Vigne et al. 2006) and are thought to have lifetimes comparable to those of arms (Elmegreen 1980). However, there are distinct differences between spurs and branches. It is generally thought that spurs extend outward from an arm into the interarm space at a large pitch angle ($\sim 60^\circ$, Elmegreen 1980), whereas branches have a smaller pitch angle (usually $< 20^\circ$) and are longer than spurs. A branch usually occurs as a bifurcation of a main spiral arm and gives rise to the main interarm features, as seen in Figures 9 and 12 of La Vigne et al. (2006). Based on our observations, the Local arm is clearly not a spur and instead may be a branch.

We estimate the pitch angle of the Local arm by fitting a straight line to the logarithm of Galactocentric radius, R_{gc} , versus Galactocentric azimuth, β (defined as 0 toward the Sun and increasing with Galactic longitude), as shown in Figure 11. We do the fitting with a Bayesian Markov chain Monte Carlo (MCMC) exploration of parameter space using the Metropolis-Hastings algorithm to accept or reject trials. Since parallax uncertainty maps into both $\ln R_{gc}$ and β , we numerically evaluate uncertainties for these parameters and then minimize residuals divided by their uncertainties projected perpendicular to the fitted line. Since the slope of the fitted line is the tangent of the pitch angle, one of the two fitted parameters, we iterate the fitting procedure until convergence before performing the final MCMC trials used to determine marginalized posteriori probability density functions for the

two parameters. See Reid et al. (in preparation) for more details. We find the pitch angle of the Local arm to be $10.1^\circ \pm 2.7^\circ$. This value is shallower than the preliminary estimate in Reid et al. (2009b) based on only five parallaxes and heavily weighted by G059.78+0.06, which may be an outlier. Our estimated spiral arm pitch angle is similar to that of the Sagittarius and Perseus arms (Wu, in preparation; Choi, in preparation) and is characteristic of major arms in Sb-Sc type galaxies (Kennicutt 1981).

Our findings suggest three possibilities for the nature of the Local arm in relation to the spiral structure of the Milky Way.

(1) It could be a branch of the Perseus arm, as suggested by many authors. Two facts support this theory. The Local arm is closer to the Perseus arm than to the Sagittarius arm, and branches often appear at the inner edge of an arm in external galaxies (Patsis et al. 1997; La Vigne et al. 2006). Extrapolating from the most distant measured star-forming region in Figure 12 (left panel) suggests that a bifurcation point could be at a distance of ≈ 6 kpc at $l \approx 55^\circ$. This location is close to that suggested by Urasin (1987) for such a branching, based on photometric distances of open star clusters.

(2) The Local arm could be part of a major arm, as suggested by Bok and Kerr (Bok 1959; Bok et al. 1970; Kerr 1970; Kerr & Kerr 1970). In their model, the Local arm runs through the Sun and connects with the Carina arm, although most authors following the GG76 model believe that the Carina arm connects to the Sagittarius arm. At present, however, the lack of parallax data for $l > 230^\circ$ precludes critically testing this theory. Figure 12 (right panel) shows the positions of optical H II regions with stellar distances in the 3rd Galactic quadrant from Russeil (2003). It is possible the Local arm connects to the Carina arm at $l \approx 282^\circ$, near its tangent point (Bronfman et al. 2000). This could be a bifurcation point where the Carina arm splits into the Local branch and the Sagittarius branch. However, since optical distances generally have large uncertainties, as shown by Russeil et al. (2007), more VLBI parallax results from the Southern Hemisphere are required before a definite conclusion can be reached.

(3) The Local arm is an independent spiral arm segment, which consists of numerous major star-forming regions, such as Cygnus X region (Rygl et al. 2012), with similar Galactocentric distances and space velocities (see Section 5). From the model of Cordes & Lazio (2002), the interarm spacing between two major arms of the Milky Way is usually more than 2 kpc, even more than 3 kpc in some places. If the Local arm is a major arm, the spacing between it and nearby arms would be only 1 – 2 kpc. However, such a small spacing is not expected from the theory of spiral density waves (Yuan 1969).

5. SPACE MOTION OF SOURCES IN THE LOCAL ARM

Combining the distances, LSR velocities and proper motions of the masers in star forming regions yields their locations in the Galaxy and their full space motions. The proper motion uncertainties for most sources listed in Table 4 are based on measurement accuracy alone. There is additional uncertainty when referring these motions to that of the central star (or stars) that excite the masers. Basically, they are 3 to 5 km s⁻¹ for CH₃OH, SiO masers and continuum emission, and 5 to 20 km s⁻¹ for H₂O masers (depending on the width/complexity of the spectrum). The v_{LSR} values are based on weighted average velocity of maser and the larger molecular cloud material (usually from CO or other thermally emitting molecule lines) of which the maser is a part. For water masers, we weighted the thermal line velocity more than water masers, while for CH₃OH and SiO masers a greater weight is given to masers, as they are much more closely tied to the central star. The uncertainties for v_{LSR} include a term that comes from the difference between a maser and its associated thermal line velocity. For continuum sources, the v_{LSR} values are based on the velocity of thermal lines and we assign uncertainties of ± 5 km s⁻¹.

Given a model for the scale and rotation of the Milky Way, we can subtract the effects of Galactic rotation and estimate peculiar (i.e. non-circular) motions. Peculiar motions are given in a Galactocentric reference frame, where U_s , V_s and W_s are the velocity components toward the Galactic center, in the direction of Galactic rotation, and toward the North Galactic Pole, respectively, at the location of a given source in the Galaxy. Details of these calculations are given in the Appendix of Reid et al. (2009b). Here we adopt recent estimates of $R_0 = 8.3$ kpc and $\Theta_0 = 239$ km s⁻¹ (Brunthaler et al. 2011), and the latest Solar motion values $U_\odot = 11.10$ km s⁻¹, $V_\odot = 12.24$ km s⁻¹ and $W_\odot = 7.25$ km s⁻¹ (Schönrich et al. 2010).

The peculiar motions of the 30 Local arm sources are shown in the Figure 13 and range from -16 to 10 km s⁻¹ towards the Galactic center and from -19 to 2 km s⁻¹ in the direction of Galactic rotation (Table 5). A weighted average of these peculiar motions indicates a systematic peculiar motion for Local arm sources of 1.3 ± 1.3 km s⁻¹ toward the Galactic center ($\overline{U_s}$), -5.4 ± 1.0 km s⁻¹ in the direction of Galactic rotation ($\overline{V_s}$), indicating counter rotation, and 2.4 ± 1.4 km s⁻¹ toward the north Galactic pole ($\overline{W_s}$). We use the standard error of the means as the uncertainties. Note that the values for U_s and V_s depend sensitively on the adopted Θ_0 and V_\odot values, respectively. From a sample of 16 HMSFRs in several spiral arms, Reid et al. (2009b) obtained $(\overline{U_s}, \overline{V_s}, \overline{W_s}) = (2, -15, -3)$ km s⁻¹ with uncertainties of ± 2 km s⁻¹. These average peculiar motions used the Solar Motion from Dehnen & Binney (1998) which had $V_\odot = 5.2$ km s⁻¹, or about 7 km s⁻¹ lower than the Schönrich et al. (2010) value. Adjusting the Reid et al. (2009b) values to the newer Solar

Motion would yield $(\overline{U}_s, \overline{V}_s, \overline{W}_s) \approx (2, -8, -3) \text{ km s}^{-1}$. Thus, the Local arm peculiar motions, on average, are consistent with those of HMSFRs in other spiral arms, further supporting our theory that the Local arm is a major structure in the Milky Way.

6. CONCLUSIONS

We have studied the nature of the Local arm by measuring parallax distances and proper motions of nine 22-GHz H₂O masers associated with star-forming regions. We include previously published parallaxes and proper motions for 21 other star forming regions (from either H₂O, CH₃OH, SiO masers or YSO continuum emission). These 30 sources clearly lie between the Sagittarius and Perseus spiral arms and belong to the Local arm. This arm is at least ~ 5 kpc in length and ~ 1 kpc in width; it is not a spur and may be a branch of the Perseus arm, a bifurcation of the Carina arm, or an independent arm segment. The average peculiar motions of the sources in the Local arm are similar to those of HMSFRs in other major spiral arms of the Milky Way.

Facilities: VLBA

We would like to thank the anonymous referee for many useful comments that have improved the paper. This work was supported by the Chinese NSF through grants NSF 11133008, NSF 11073054, NSF 11203082, BK2012494, and the Key Laboratory for Radio Astronomy, CAS. This research has made use of the SIMBAD database, operated at CDS, Strasbourg, France.

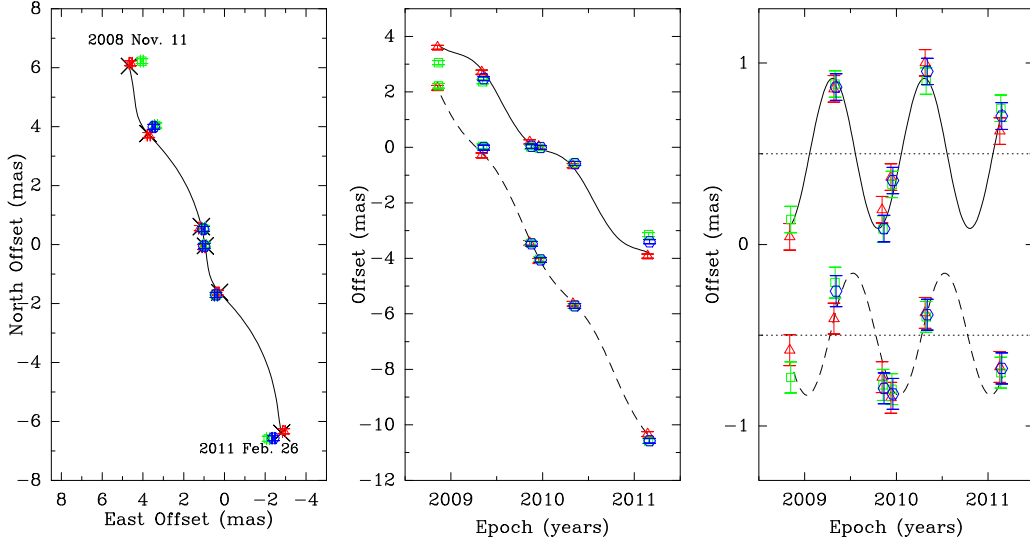


Fig. 1.— Parallax and proper motion data and fits for ON 1. Plotted are position offsets for one maser spot at $V_{\text{LSR}} = 14.8$ (red triangles) and two maser spots at 10.6 km s^{-1} (green squares for the strong spot and blue hexagons for the weak spot) relative to the background source J2003+3034. *Left Panel:* Positions in the sky with the first and last epochs labeled. The expected positions from the parallax and proper motion fit are indicated (crosses). *Middle Panel:* East (solid line) and north (dashed line) position offsets and best parallax and proper motions fits versus time. *Right Panel:* Same as the *middle panel* but with the best-fit proper motions removed for clearer illustration of the parallax sinusoid.

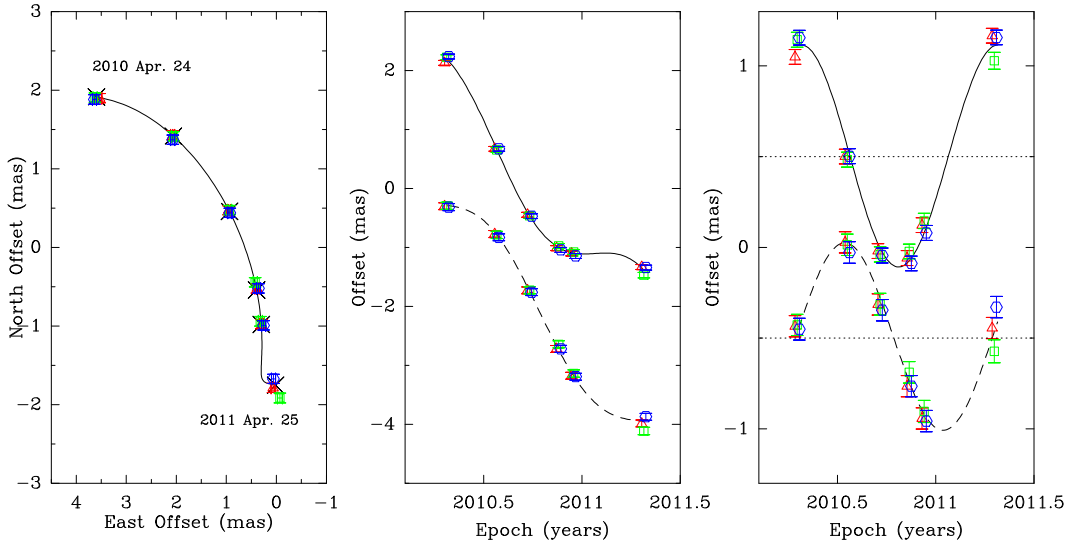


Fig. 2.— Parallax and proper motion data and fits for G074.03–01.71. Plotted are position offsets for three maser spots at $V_{\text{LSR}} = 13.4$ (red triangles), 12.9 (green square) and 12.5 km s^{-1} (blue hexagons) relative to the background source J2025+3343. Solid and dashed lines in the three panels represent the same fits as in the corresponding panels of Fig. 1.

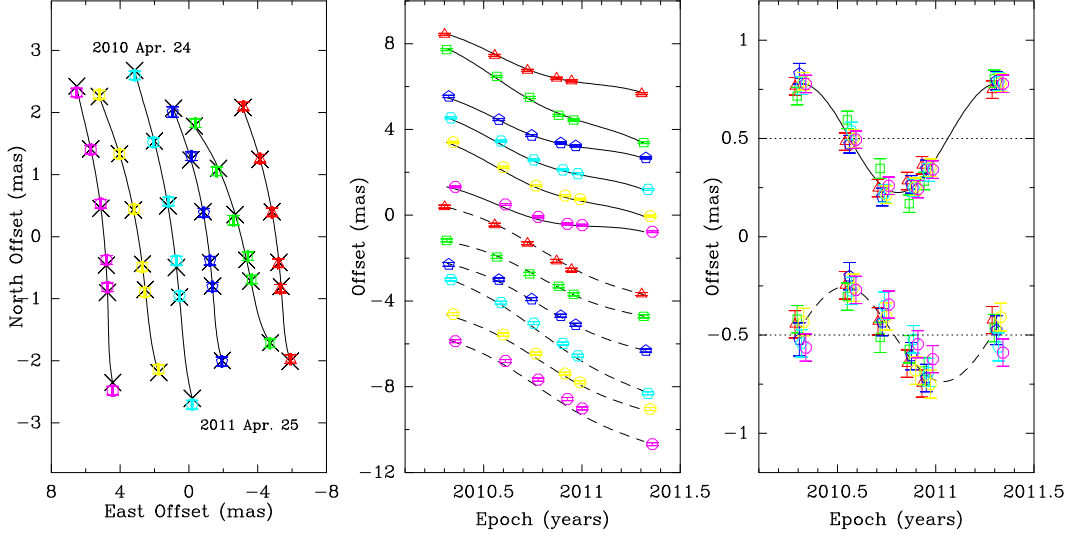


Fig. 3.— Parallax and proper motion data and fits for G075.76+00.33. Plotted are position offsets of 6 maser spots at $V_{\text{LSR}} = -5.0$ (red triangles), -7.1 (green square), -9.2 (blue pentagons), -9.6 (cyan hexagons), -10.4 (yellow heptagons), and -11.3 km s^{-1} (fuchsia octagons) relative to the background source J2015+3710. Solid and dashed lines in the three panels represent the same fits as in the corresponding panels of Fig. 1.

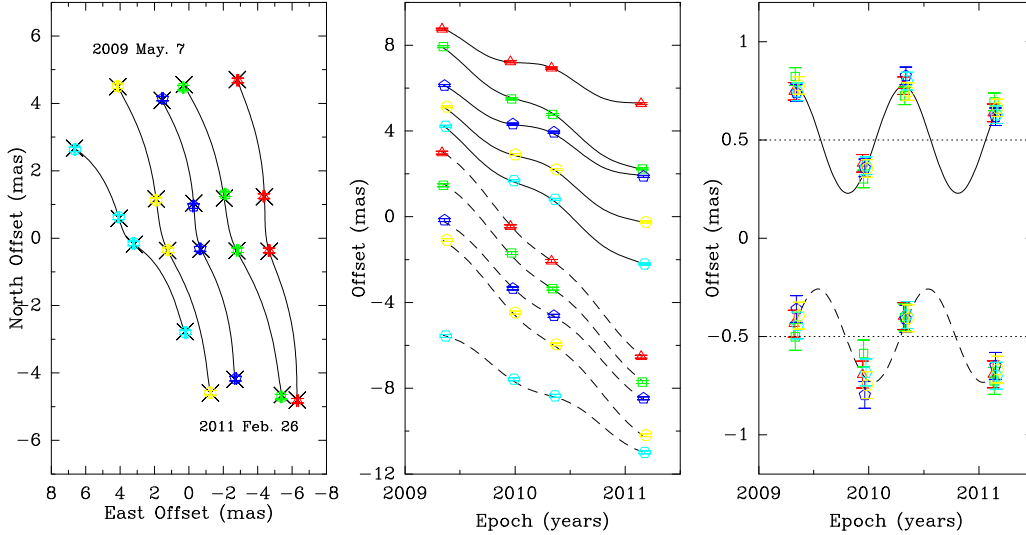


Fig. 4.— Parallax and proper motion data and fits for G075.78+00.34. Plotted are position offsets of 5 maser spots at $V_{\text{LSR}} = 0.4$ (red triangles), 2.9 (green square), 3.4 (blue pentagons), 3.8 (cyan hexagons), and 4.2 (yellow heptagons) relative to the background source J2015+3710. Solid and dashed lines in the three panels represent the same fits as in the corresponding panels of Fig. 1.

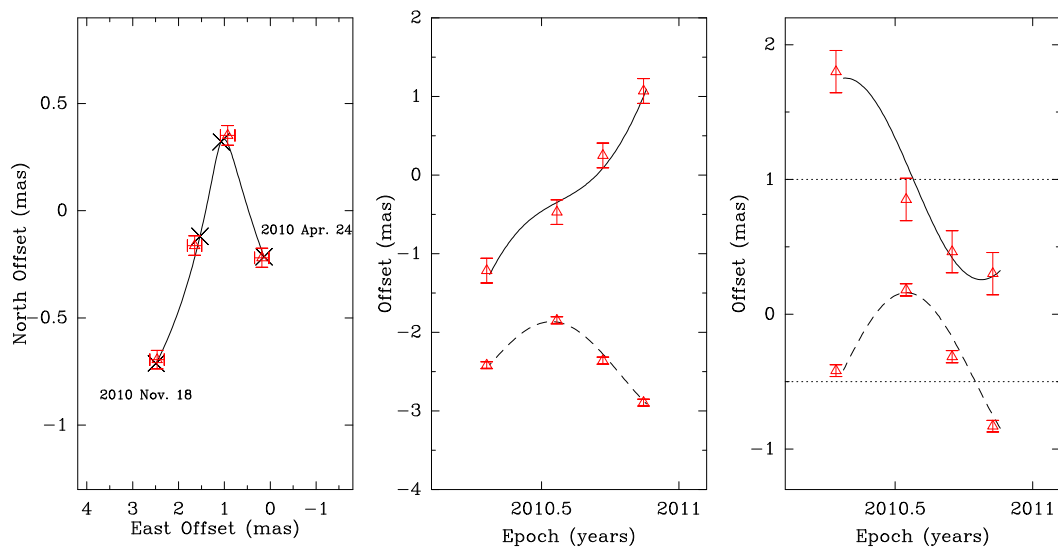


Fig. 5.— Parallax and proper motion data and fits for G076.38–00.61. Plotted are position offsets of the maser spot at $V_{\text{LSR}} = 6.9 \text{ km s}^{-1}$ (red triangles) relative to the background source J2015+3710. Solid and dashed lines in the three panels represent the same fits as in the corresponding panels of Fig. 1.

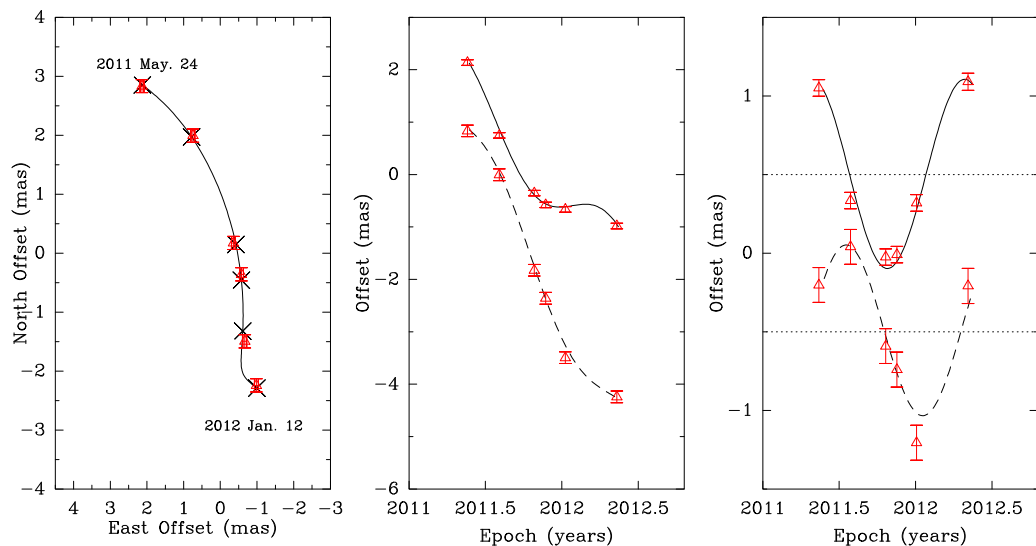


Fig. 6.— Parallax and proper motion data and fits for G079.87+01.17. Plotted are position offsets of the maser spot at $V_{\text{LSR}} = -4.6 \text{ km s}^{-1}$ (red triangles) relative to the background source J2007+4029. Solid and dashed lines in the three panels represent the same fits as in the corresponding panels of Fig. 1.

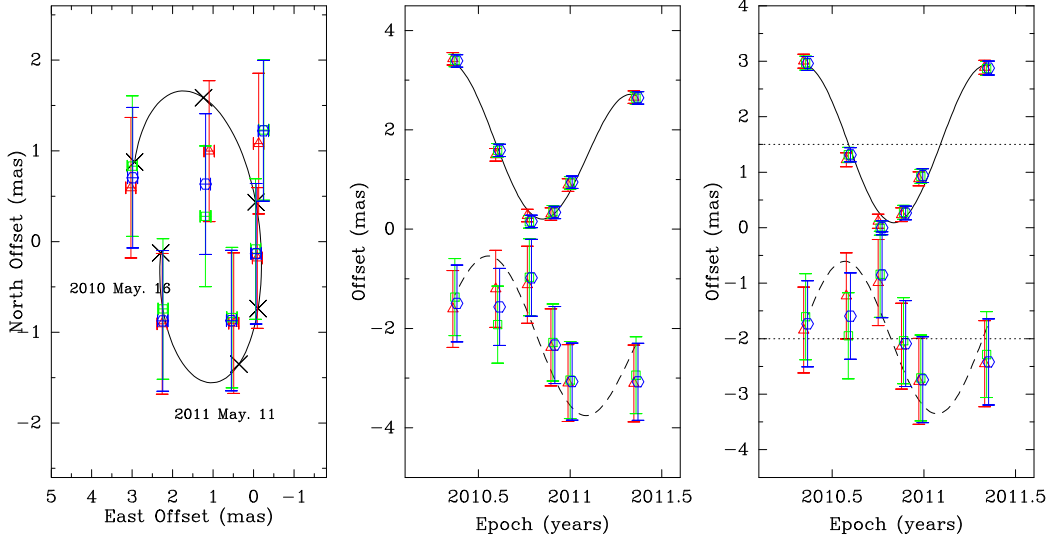


Fig. 7.— Parallax and proper motion data and fits for G090.21+02.32. Plotted are position offsets of the maser spot at $V_{\text{LSR}} = -6.2 \text{ km s}^{-1}$ relative to three background sources J2114+4953 (red triangles), J2056+4940 (green squares), and J2059+4851 (blue hexagons), respectively. Solid and dashed lines in the three panels represent the same fits as in the corresponding panels of Fig. 1.

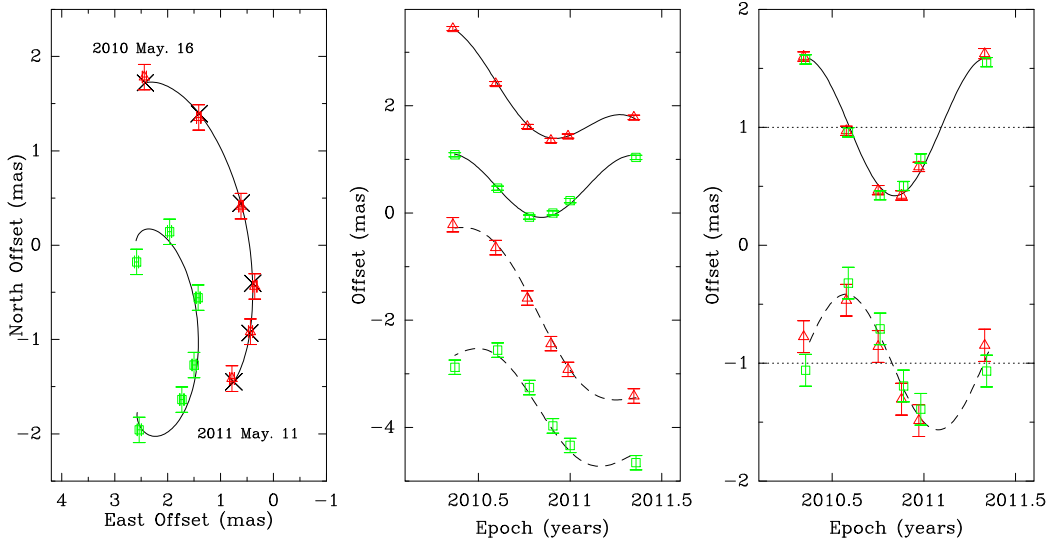


Fig. 8.— Parallax and proper motion data and fits for G092.67+03.07. Plotted are position offsets of the maser spot at $V_{\text{LSR}} = -3.7$ (red triangles) and -14.3 km s^{-1} (green square) relative to the background sources J2117+5431. Solid and dashed lines in the three panels represent the same fits as in the corresponding panels of Fig. 1.

Table 4. Parallaxes and Proper Motions for the Local arm

| Source | ℓ (deg) | b (deg) | Parallax (mas) | μ_x (mas y ⁻¹) | μ_y (mas y ⁻¹) | v_{LSR} (km s ⁻¹) | Ref. |
|----------------------------------|-----------------|--------------|-------------------|-----------------------------------|-----------------------------------|---|------------|
| EC95/Serpens | 31.5615 | +5.3303 | 2.410 ± 0.020 | +0.70 ± 0.02 | -3.64 ± 0.10 | 7 ± 5 | 5,8 |
| G059.78+00.06 | 59.7829 | +0.0647 | 0.463 ± 0.020 | -1.65 ± 0.03 | -5.12 ± 0.08 | 25 ± 3 | 25,32 |
| ON 1 ^a | 69.5402 | -0.9755 | 0.406 ± 0.031 | -3.19 ± 0.37 | -5.22 ± 0.25 | 12 ± 5 | 1,24,25,27 |
| G074.03-01.71 | 74.0343 | -1.7140 | 0.629 ± 0.017 | -3.79 ± 0.18 | -4.88 ± 0.25 | 5 ± 5 | 1,4 |
| G075.76+00.33 | 75.7610 | +0.3400 | 0.285 ± 0.022 | -3.08 ± 0.06 | -4.56 ± 0.08 | -9 ± 9 | 1,25 |
| G075.78+00.34/ON 2N ^b | 75.7821 | +0.3428 | 0.271 ± 0.022 | -2.79 ± 0.10 | -4.69 ± 0.12 | 1 ± 5 | 1,2,25 |
| G076.38-00.61 | 76.3809 | -0.6177 | 0.770 ± 0.053 | -3.73 ± 3.00 | -3.84 ± 3.00 | -2 ± 5 | 1,4 |
| IRAS 20126+4104 ^c | 78.1224 | +3.6328 | 0.610 ± 0.020 | -4.14 ± 0.13 | -4.14 ± 0.13 | -4 ± 5 | 4,22 |
| AFGL 2591 | 78.8867 | +0.7090 | 0.300 ± 0.010 | -1.20 ± 0.32 | -4.80 ± 0.12 | -6 ± 7 | 25,28 |
| IRAS 20290+4052 | 79.7358 | +0.9905 | 0.737 ± 0.062 | -2.84 ± 0.09 | -4.14 ± 0.54 | -3 ± 5 | 4,28 |
| G079.87+01.17 | 79.8769 | +1.1770 | 0.620 ± 0.027 | -3.23 ± 1.31 | -5.19 ± 1.31 | -5 ± 10 | 1,4 |
| NML Cyg | 80.7984 | -1.9209 | 0.620 ± 0.047 | -1.55 ± 0.42 | -4.59 ± 0.41 | -3 ± 3 | 15,34 |
| DR 20 | 80.8615 | +0.3834 | 0.687 ± 0.038 | -3.29 ± 0.13 | -4.83 ± 0.26 | -3 ± 5 | 4,28 |
| DR 21 | 81.7524 | +0.5908 | 0.666 ± 0.035 | -2.84 ± 0.15 | -3.80 ± 0.22 | -3 ± 3 | 7,28 |
| W 75N | 81.8713 | +0.7807 | 0.772 ± 0.042 | -1.97 ± 0.10 | -4.16 ± 0.15 | 7 ± 3 | 25,28 |
| G090.21+02.32 | 90.2105 | +2.3244 | 1.483 ± 0.038 | -0.67 ± 3.13 | -0.90 ± 3.13 | -3 ± 5 | 1,4 |
| G092.67+03.07 | 92.6712 | +3.0712 | 0.613 ± 0.020 | -0.69 ± 0.26 | -2.25 ± 0.33 | -5 ± 10 | 1,4 |
| G105.41+09.87 | 105.4154 | +9.8783 | 1.129 ± 0.063 | -0.21 ± 2.38 | -5.49 ± 2.38 | -10 ± 5 | 1,25 |
| IRAS 22198+6336 | 107.2982 | +5.6398 | 1.309 ± 0.047 | -2.47 ± 0.21 | +0.26 ± 0.40 | -11 ± 5 | 4,10,13 |
| L 1206 | 108.1845 | +5.5188 | 1.289 ± 0.153 | +0.27 ± 0.23 | -1.40 ± 1.95 | -11 ± 3 | 20,27 |
| Cep A | 109.8713 | +2.1143 | 1.430 ± 0.080 | +0.50 ± 1.10 | -3.70 ± 0.20 | -7 ± 5 | 21,25 |
| L 1287 | 121.2978 | +0.6588 | 1.077 ± 0.039 | -0.86 ± 0.11 | -2.29 ± 0.56 | -23 ± 5 | 25,27 |
| L 1448 C | 158.0625 | -21.4203 | 4.310 ± 0.330 | +21.90 ± 0.70 | -23.10 ± 3.30 | 10 ± 7 | 3,12 |
| SVS 13/NGC 1333 | 158.3474 | -20.5551 | 4.250 ± 0.320 | +14.25 ± 1.30 | -8.95 ± 1.75 | 7 ± 3 | 11,29 |
| Orion ^d | 209.0071 | -19.3854 | 2.408 ± 0.033 | +3.30 ± 1.50 | +0.10 ± 1.50 | 3 ± 5 | 9,16,19,31 |
| G232.62+00.99 | 232.6205 | +0.9956 | 0.596 ± 0.035 | -2.17 ± 0.06 | +2.09 ± 0.46 | 21 ± 3 | 4,26 |
| VY CMa ^e | 239.3526 | -5.0655 | 0.855 ± 0.080 | -2.80 ± 0.20 | +2.60 ± 0.20 | 20 ± 3 | 6,23,33 |
| DoAr21/Ophiuchus | 353.0157 | +16.9815 | 8.200 ± 0.370 | -26.47 ± 0.92 | -28.23 ± 0.73 | 3 ± 5 | 17,18 |
| S1/Ophiuchus | 353.0992 | +16.8943 | 8.550 ± 0.500 | -3.88 ± 0.87 | -31.55 ± 0.69 | 3 ± 5 | 17,18 |
| IRAS 16293-2422 | 353.9354 | +15.8393 | 5.600 ± 1.500 | -20.60 ± 0.70 | -32.40 ± 2.00 | 4 ± 3 | 14,30 |

Note. — Columns 2 and 3 give Galactic longitude and latitude, respectively. Columns 5 and 6 are proper motion in the eastward ($\mu_x = \mu_\alpha \cos \delta$) and northward directions ($\mu_y = \mu_\delta$), respectively. Column 7 lists LSR velocity components of molecular line emission; these can be converted to a heliocentric frame as described in the Appendix of Reid et al. (2009b).

Note. — References are 1: this paper; 2: Ando et al. (2011); 3: Bachiller et al. (1990) CS (1-0); 4: Bronfman et al. (1996) CS (2-1); 5: Choi et al. (1999) HCO⁺ (1-0); 6: Choi et al. (2008); 7: Dickel et al. (1978) CO (1-0); 8: Dzib et al. (2010); 9: Hirota et al. (2007); 10: Hirota et al. (2008a); 11: Hirota et al. (2008b); 12: Hirota et al. (2011); 13: Honma et al. (2012); 14: Imai et al. (2007); 15: Kemper et al. (2003) CO (4-3); 16: Kim et al. (2008); 17: Loinard et al. (2008); 18: Loren (1989) ¹³CO (1-0); 19: Menten et al. (2007); 20: Molinari et al. (1996) NH₃ (1,1)(2,2); 21: Moscadelli et al. (2009); 22: Moscadelli et al. (2011); 23: Muller et al. (2007) CO (2-1); 24: Nagayama et al. (2011); 25: Plume et al. (1992) CS (7-6); 26: Reid et al. (2009a); 27: Rygl et al. (2010); 28: Rygl et al. (2012); 29: Snell & Edwards (1981) CO (1-0); 30: Takakuwa et al. (2007) HCN (4-3); 31: Wiseman & Ho (1998) NH₃ (1,1); 32: Xu et al. (2009); 33: Zhang et al. (2012a); 34: Zhang et al. (2012b)

^aThe parallax and proper motions of ON 1 are unweighted average values of the independent results from Rygl et al. (2010), Nagayama et al. (2011) and this paper.

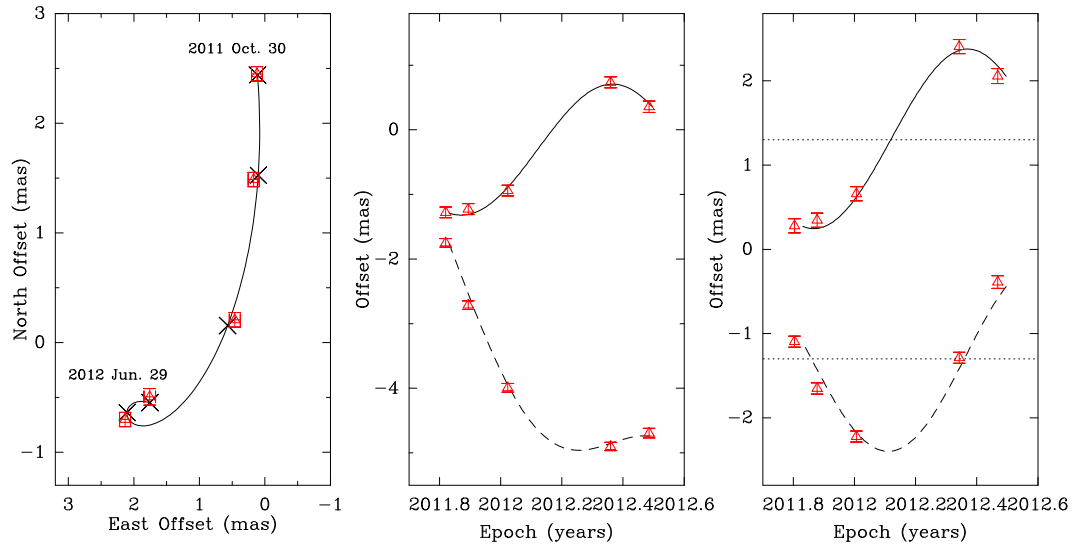


Fig. 9.— Parallax and proper motion data and fits for G105.41+09.87. Plotted are position offsets of the maser spot at $V_{\text{LSR}} = -12.1 \text{ km s}^{-1}$ (red triangles) relative to the background source J2203+6750. Solid and dashed lines in the three panels represent the same fits as in the corresponding panels of Fig. 1.

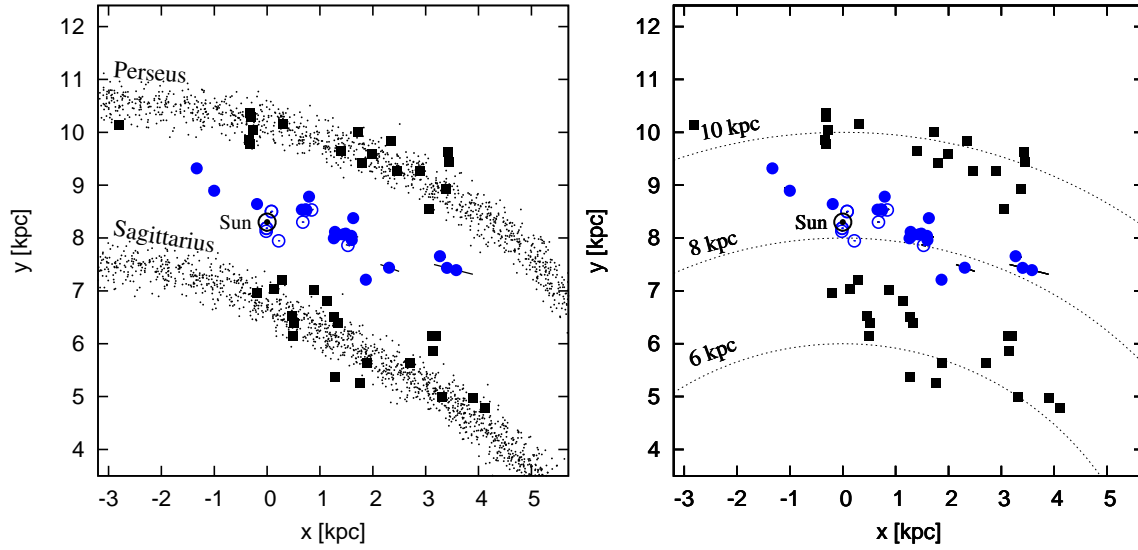


Fig. 10.— Location of 30 sources (dots) determined by trigonometric parallaxes in the Local arm. The filled dots represent HMSFRs, while the unfilled ones represent low- or intermediate-mass star-forming regions. The black squares represent some parallax data in the Perseus and Sagittarius arm. Distance error bars of the Local arm sources are indicated, but most are smaller than the symbols. The Galaxy is viewed from the north galactic pole with the Galactic center (not shown) located at (0, 0) kpc. The Sun is located at (0, 8.3) kpc and marked by a black circle around a dot. The background (left panel) is a model of the Milky Way of Cordes & Lazio (2002), while the lines (right panel) are constant radius. [See the electronic edition of the Journal for a color version of this figure.]

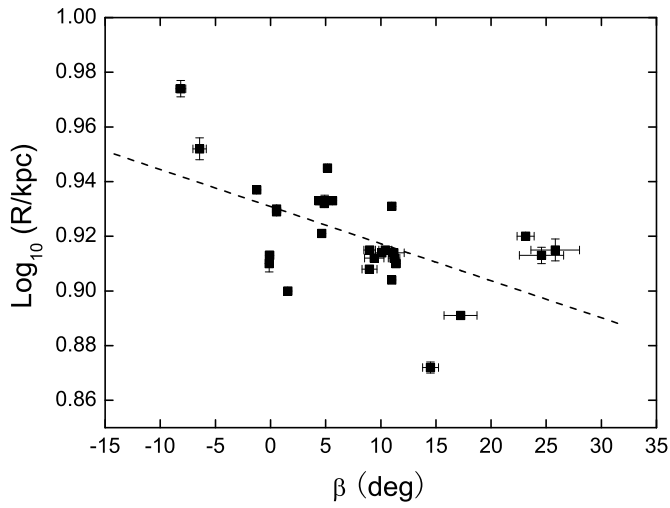


Fig. 11.— Pitch angle of the Local arm. The logarithm of Galactocentric radius R (in kpc units) is plotted against Galactocentric azimuth β , defined as zero toward the Sun and increasing with increasing Galactic longitude. Data based on trigonometric parallaxes for sources in Table 4 are shown along with 1σ uncertainties. Positional variations of these sources are clearly greater than the parallax uncertainties. The fit line to the data (including all sources) is shown with dashed line. Pitch angle is proportional to the negative of the arctangent of the line slope and we estimate a pitch angle of $10.1^\circ \pm 2.7^\circ$.

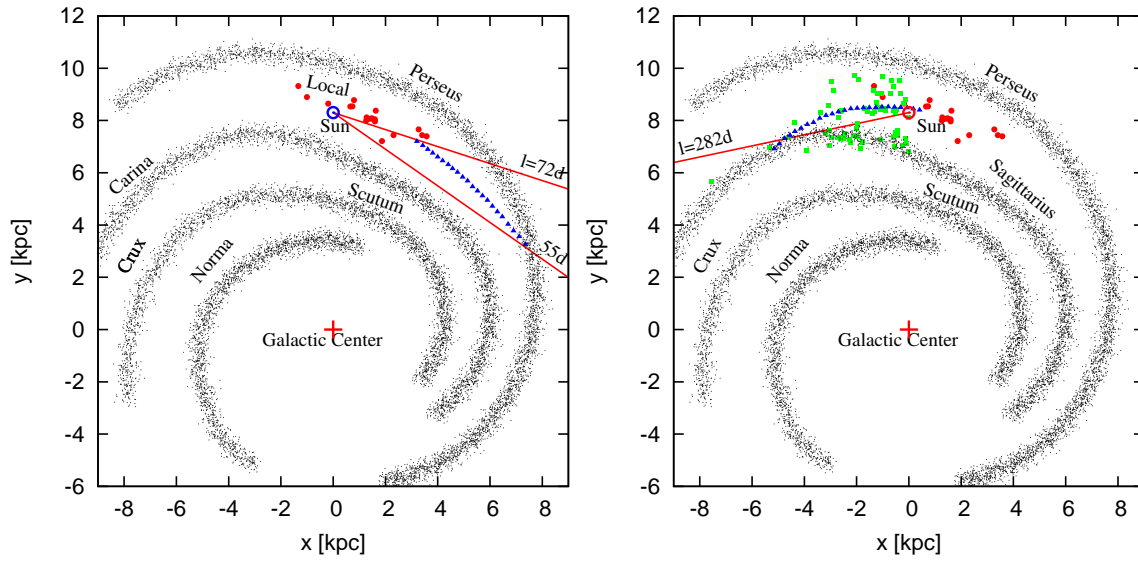


Fig. 12.— Two possible models of the Local arm. Red dots represent the parallax data in Table 4. Blue triangles represent two possible models of the Local arm. Green squares represent stellar distances (Russeil 2003; Russeil et al. 2007). The background is a model of the Milky Way of Cordes & Lazio (2002). [See the electronic edition of the Journal for a color version of this figure.]

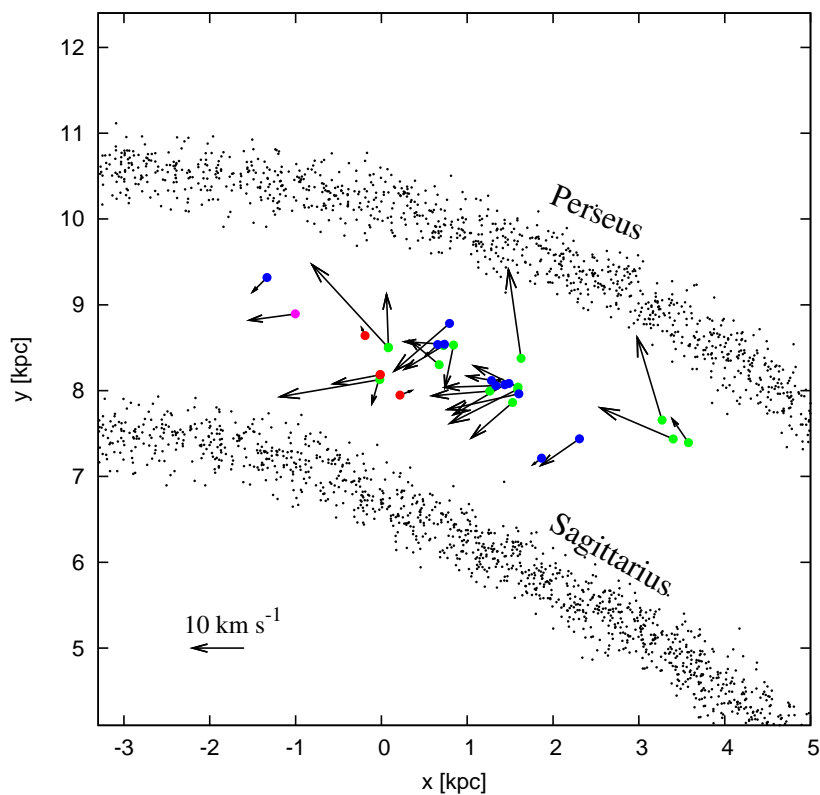


Fig. 13.— Peculiar motion vectors of methanol (blue dots), water (green dots), SiO (pink dot) masers, and continuum emission sources (red dots) in the Local arm after transforming to a reference frame rotating with the galaxy, using values of $R_0 = 8.3$ kpc and $\Theta_0 = 239$ km s $^{-1}$ (Brunthaler et al. 2011). A motion scale of 10 km s $^{-1}$ is indicated in the bottom left corner of the panels. The background is a model of the Milky Way of Cordes & Lazio (2002). The galaxy is viewed from the north galactic pole, it rotates clockwise, and the Sun is at (0,8.3) kpc. [See the electronic edition of the Journal for a color version of this figure.]

^bThe parallax and proper motions of G075.78+00.34 is unweighted average value of the independent results from Ando et al. (2011) and this paper.

^cThe proper motion of IRAS 20126+4104 is from its methanol masers (Moscadelli, private communication).

^dThe parallax of Orion is an unweighted average value of the independent results from Menten et al. (2007) and Kim et al. (2008) with equal accuracy, while the proper motions come from Menten et al. (2007), because Hirota et al. (2007) and Kim et al. (2008) only use one spot to estimate these values.

^eThe parallax of VY CMa is unweighted average value of the independent results from Choi et al. (2008) and Zhang et al. (2012a), while the proper motions come from Zhang et al. (2012a) because Choi et al. (2008) only use one spot to estimate these values.

REFERENCES

- Ando, K., Nagayama, T., Omodaka, T., et al. 2011, *PASJ*, 63, 45
- Avedisova, V. S. 1985, *Soviet Astronomy Letters*, 11, 185
- Bachiller, R., Martin-Pintado, J., Tafalla, M., Cernicharo, J., & Lazareff, B. 1990, *A&A*, 231, 174
- Bok, B. J. 1959, *The Observatory*, 79, 58
- Bok, B. J., Hine, A. A., & Miller, E. W. 1970, in *IAU Symp. 38, The Spiral Structure of our Galaxy*, ed. W. Becker & G. Contopoulos, p.246
- Bronfman, L., Nyman, L.-A., & May, J. 1996, *A&AS*, 115, 81
- Bronfman, L., May, J., & Luna, A. 2000, in *ASP Conf. Ser. 217, Imaging at Radio through Submillimeter Wavelengths*, ed. J. G. Mangum & S. J. E. Radford, p.66
- Brunthaler, A., Reid, M. J., Menten, K. M., et al. 2011, *AN*, 332, 461
- Carral, P., Kurtz, S. E., Rodríguez, L. F., De Pree, C., & Hofner, P. 1997, *ApJ*, 486, L103
- Choi, M., Panis, J.-F., & Evans, II, N. J. 1999, *ApJS*, 122, 519
- Choi, Y. K., Hirota, T., Honma, M., et al. 2008, *PASJ*, 60, 1007
- Churchwell, E., Babler, B. L., Meade, M. R., et al. 2009, *PASP*, 121, 213
- Clark, F. O. 1986, *A&A*, 164, L19
- Codella, C., Cesaroni, R., López-Sepulcre, A., et al. 2010, *A&A*, 510, A86
- Cordes, J. M., & Lazio, T. J. W. 2002, *arXiv:astro-ph/0207156*
- Dame, T. M., Hartmann, D., & Thaddeus, P. 2001, *ApJ*, 547, 792
- Deller, A. T., Tingay, S. J., Bailes, M., & West, C. 2007, *PASP*, 119, 318D
- Di Francesco, J., Johnstone, D., Kirk, H., MacKenzie, T., & Ledwosinska, E. 2008, *ApJS*, 175, 277
- Dickel, J. R., Dickel, H. R., & Wilson, W. J. 1978, *ApJ*, 223, 840
- Dehnen, W., & Binney, J. J. 1998, *MNRAS*, 298, 387

Table 5. Peculiar Motion of Sources in the Local arm

| Source | U_s (km s^{-1}) | V_s (km s^{-1}) | W_s (km s^{-1}) | Emission |
|---------------------|---------------------------------|---------------------------------|---------------------------------|----------|
| EC95/Serpens | -0.9 ± 4.4 | 2.2 ± 3.5 | 1.8 ± 0.8 | C |
| G059.78+00.06 | 1.5 ± 3.1 | -1.2 ± 3.6 | -4.2 ± 0.9 | M |
| ON1 | 7.1 ± 4.7 | -5.6 ± 5.5 | 5.3 ± 4.0 | M,W |
| G074.03–01.71 | 8.3 ± 2.8 | -6.5 ± 5.4 | 9.7 ± 1.7 | W |
| G075.76+00.33 | 0.4 ± 4.7 | -15.5 ± 9.2 | 6.0 ± 1.3 | W |
| G075.78+00.34/ON 2N | -2.8 ± 5.1 | -4.9 ± 5.6 | 0.5 ± 2.1 | W |
| G076.38–00.61 | 2.7 ± 18.6 | -10.8 ± 5.6 | 12.4 ± 18.6 | W |
| IRAS 20126+4104 | 5.7 ± 2.5 | -13.0 ± 5.4 | 14.9 ± 1.3 | M,W |
| AFGL 2591 | -12.8 ± 5.4 | -10.7 ± 7.1 | -22.2 ± 4.4 | W |
| IRAS 20290+4052 | 1.9 ± 3.5 | -9.8 ± 5.5 | 6.0 ± 2.2 | M |
| G079.87+01.17 | 9.1 ± 10.2 | -11.5 ± 10.2 | 3.4 ± 10.2 | W |
| NML Cyg | -2.4 ± 4.0 | -9.1 ± 3.7 | -4.8 ± 3.4 | W |
| DR 20 | 7.5 ± 2.6 | -8.8 ± 5.4 | 5.1 ± 1.5 | M |
| DR 21 | 0.0 ± 2.6 | -8.3 ± 3.6 | 6.6 ± 1.4 | M |
| W 75N | -0.5 ± 2.2 | 1.7 ± 3.7 | 1.2 ± 1.0 | M |
| G090.21+02.32 | -4.1 ± 10.1 | -5.9 ± 5.5 | 6.2 ± 10.0 | W |
| G092.67+03.07 | -16.4 ± 4.0 | -5.6 ± 10.0 | -1.7 ± 2.4 | W |
| G105.41+09.87 | 8.4 ± 9.7 | -0.8 ± 6.4 | -13.2 ± 10.0 | W |
| IRAS 22198+6336 | 5.2 ± 2.6 | -7.1 ± 5.1 | 10.6 ± 1.5 | W |
| L1206 | 0.1 ± 4.4 | -7.7 ± 4.0 | 0.1 ± 6.3 | M |
| Cep A | 2.5 ± 4.0 | -2.3 ± 5.2 | -5.2 ± 1.9 | M |
| L1287 | 10.2 ± 3.4 | -9.9 ± 4.6 | -3.0 ± 2.6 | M |
| L 1448 C | -16.0 ± 6.2 | -15.0 ± 4.8 | -4.4 ± 3.8 | W |
| SVS 13/NGC 1333 | -10.2 ± 3.0 | -0.4 ± 3.2 | 4.1 ± 2.1 | W |
| Orion | -1.4 ± 4.7 | -0.7 ± 4.1 | 5.8 ± 3.3 | C |
| G232.62+00.99 | 2.4 ± 3.6 | -3.1 ± 3.9 | 0.8 ± 2.0 | M |
| VY CMa | 0.2 ± 2.7 | -9.1 ± 3.4 | -3.2 ± 1.5 | S |
| DoAr21/Ophiuchus | 1.7 ± 4.9 | -9.1 ± 2.5 | 5.8 ± 1.7 | C |
| S1/Ophiuchus | 5.7 ± 4.9 | -1.7 ± 2.4 | -4.4 ± 1.7 | C |
| IRAS 16293-2422 | 3.3 ± 3.3 | -19.2 ± 15.4 | 1.1 ± 2.7 | W |

Note. — C, M, W, and S denote peculiar motion derived from continuum emission of YSOs, methanol masers, water masers, and silicon monoxide masers, respectively. These motions assume $R_0 = 8.3$ kpc and $\Theta_0 = 239$ km s^{-1} (Brunthaler et al. 2011), and Solar Motion values $U_\odot = 11.10$ km s^{-1} $V_\odot = 12.24$ km s^{-1} and $W_\odot = 7.25$ km s^{-1} (Schönrich et al. 2010)

- Dzib, S., Loinard, L., Mioduszewski, A. J., et al. 2010, *ApJ*, 718, 610
- Eiroa, C., Elsaesser, H., & Lahulla, J. F. 1979, *A&A*, 74, 89
- Elmegreen, D. M. 1980, *ApJ*, 242, 528
- Fomalont, E. B., Petrov, L., MacMillan, D. S., Gordon, D., & Ma, C. 2003, *AJ*, 126, 2562
- Garay, G., Rodriguez, L. F., Moran, J. M., & Churchwell, E. 1993, *ApJ*, 418, 368
- Georgelin, Y. M., & Georgelin, Y. P. 1976, *A&A*, 49, 57,
- Harju, J., Lehtinen, K., Booth, R. S., & Zinchenko, I. 1998, *A&AS*, 132, 211
- Hirota, T., Honma, M., Imai, H., et al. 2011, *PASJ*, 63, 1
- Hirota, T., Ando, K., Bushimata, T., et al. 2008a, *PASJ*, 60, 961
- Hirota, T., Bushimata, T., Choi, Y. K., et al. 2008b, *PASJ*, 60, 37
- Hirota, T., Bushimata, T., Choi, Y. K., et al. 2007, *PASJ*, 59, 897
- Hofner, P., & Churchwell, E. 1996, *A&AS*, 120, 283
- Honma, M., Nagayama, T., Ando, K., et al. 2012, *PASJ*, 64, 136H
- Hou, L. G., Han, J. L., & Shi, W. B. 2009, *A&A*, 499, 473
- Imai, H., Nakashima, K., Bushimata, T., et al. 2007, *PASJ*, 59, 1107
- Immer, K., Brunthaler, A., Reid, M. J., et al. 2011, *ApJS*, 194, 25
- Kemper, F., Stark, R., Justtanont, K., et al. 2003, *A&A*, 407, 609
- Kennicutt, R. C., Jr. 1981, *AJ*, 86, 1847
- Kerr, F. J. 1970, in *IAU Symp. 38, The Spiral Structure of our Galaxy*, ed. W. Becker & G. Contopoulos, p.95
- Kerr, F. J., & Kerr, M. 1970, *ApJ*, 6, 175
- Kim, M. K., Hirota, T., Honma, M., et al. 2008, *PASJ*, 60, 991
- Kumar, M. S. N., Tafalla, M., & Bachiller, R. 2004, *A&A*, 426, 195
- Kurtz, S., Churchwell, E., & Wood, D. O. S. 1994, *ApJS*, 91, 659

- Kurtz, S., Hofner, P., & Álvarez, C. V. 2004, *ApJS*, 155, 149
- La Vigne, M. A., Vogel, S. N., & Ostriker, E. C. 2006, *ApJ*, 650, 818
- Liszt, H. S. 1985, in *IAU Symp. 106, The Milky Way Galaxy*, ed. H. van Woerden et al., p.283
- Loinard, L., Torres, R. M., Mioduszewski, A. J., & Rodríguez, L. F. 2008, *ApJ*, 675L, 29
- Loren, R. B. 1989, *ApJ*, 338, 902
- Ma, C., Arias, E. F., Eubanks, T. M., et al. 1998, *AJ*, 116, 516
- Maucherat, A. J. 1975, *A&A*, 45, 193
- Mao, R. Q., Yang, J., Henkel, C., & Jiang, Z. B. 2002, *A&A*, 389, 589
- Menten, K. M., Reid, M. J., Forbrich, J., & Brunthaler, A. 2007, *A&A*, 474, 515
- Molinari, S., Brand, J., Cesaroni, R., & Palla, F. 1996, *A&A*, 308, 573
- Molinari, S., Brand, J., Cesaroni, R., Palla, F., & Palumbo, G. G. C. 1998, *A&A*, 336, 339
- Morgan, W. W., Sharpless, S., & Osterbrock, D. 1952, *AJ*, 57, 3
- Morgan, W. W., Whitford, A. E., & Code, A. D. 1953, *ApJ*, 118, 318
- Moscadelli, L., Reid, M. J., Menten, K. M., et al. 2009, *ApJ*, 693, 406
- Moscadelli, L., Cesaroni, R., Rioja, M. J., Dodson, R., & Reid, M. J. 2011, *A&A*, 526, 66
- Muller, S., Dinh-V-Trung, Lim, J., Hirano, N., Muthu, C., & Kwok, S. 2007, *ApJ*, 656, 1109
- Nagayama, T., Omodaka, T., Nakagawa, A., et al. 2011, *PASJ*, 63, 23
- Oort, J. H., Kerr, F. J., & Westerhout, G. 1958, *MNRAS*, 118, 379
- Palla, F., Cesaroni, R., Brand, J., et al. 1993, *A&A*, 280, 599
- Patsis P. A., Grosbol P., & Hiotelis N. 1997, *A&A*, 323, 762
- Petrov, L., Kovalev, Y. Y., Fomalont, E., & Gordon, D. 2005, *AJ*, 129, 1163
- Plume, R., Jaffe, D. T., & Evans, II, N. J. 1992, *ApJS*, 78, 505
- Racine, R. 1968, *AJ*, 73, 233

- Reid, M. J. , Menten, K. M., Brunthaler, A., et al. 2009a, ApJ, 693, 397
- Reid, M. J., Menten, K. M., Zheng, X. W., et al. 2009b, ApJ, 700, 137
- Russeil, D. 2003, A&A, 397, 133
- Russeil, D., Adami, C., & Georgelin, Y. M. 2007, A&A, 470, 161
- Rygl, K. L. J., Brunthaler, A., Reid, M. J., et al. 2010, A&A, 511, 2
- Rygl, K. L. J., Brunthaler, A., Sanna, A., et al. 2012, A&A, 539, 79
- Schneider, N., Simon, R., Bontemps, S., Comerón, F., & Motte, F. 2007, A&A, 474, 873
- Schneider, N., Simon, R., Kramer, C., Stutzki, J., & Bontemps, S. 2002, A&A, 384, 225
- Schönrich, R., Binney, J. J., & Dehnen, W. 2010, MNRAS, 403, 1829
- Scoville, N. Z., Polletta, M., Ewald, S., Stolovy, S. R., Thompson, R., & Rieke, M. 2001, AJ, 122, 3017
- Shevchenko, V. S., & Yabukov, S. D. 1989, Soviet Ast., 33, 370
- Slysh, V. I., Dzura, A. M., Val'tts, I. E., & Gerard, E. 1997, A&AS, 124, 85
- Smith, N., Jones, T. J., Gehrz, R. D., Klebe, D., & Creech-Eakman, M. J. 2001, AJ, 121, 984
- Snell, R. L., & Edwards, S. 1981, ApJ, 251, 103
- Steiman-Cameron, T. Y. 2010, in a conf. in honour of K. C. Freeman, Galaxies and their Masks, ed. D. L. Block et al., p. 45
- Takakuwa, S., Ohashi, N., Bourke, T. L., et al. 2007, ApJ, 662, 431
- Taylor, J. H., & Cordes J. M. 1993, ApJ, 411, 674
- Trinidad, M. A., Curiel, S., Torrelles, J. M., et al. 2004, ApJ, 613, 416
- Urasin, L. A. 1987, Soviet Astronomy Letters, 13, 356
- Vallée, J. P. 2002, ApJ, 566, 261
- van der Walt, D. J., Retief, S. J. P., Gaylard, M. J., & MacLeod, G. C. 1996, MNRAS, 282, 1085

- Weintraub, D. A., Kastner, J. H., & Mahesh, A. 1994, *ApJ*, 420, 187
- Wiseman, J. J., & Ho, P. T. P. 1998, *ApJ*, 502, 676
- Wouterloot, J. G. A., & Brand J. 1989, *A&AS*, 80, 149
- Wood, D. O. S., & Churchwell, E. 1989a, *ApJ*, 340, 265
- Wood, D. O. S., & Churchwell, E. 1989b, *ApJS*, 69, 831
- Xu, Y., Reid, M. J., Menten, K. M., & Zheng, X. W. 2006a, *ApJS*, 166, 526
- Xu, Y., Shen, Z.-Q., Yang, J., et al. 2006b, *AJ*, 132, 20
- Xu, Y., Reid, M. J., Menten, K. M., et al. 2009, *ApJ*, 693, 413
- Yang, J., Jiang, Z. B., Wang, M., Ju, B. G., & Wang, H. C. 2002, *ApJS*, 141, 157
- Yuan, C. 1969, *ApJ*, 158, 871
- Zhang, B., Reid, M. J., Menten, K. M., & Zheng, X. W. 2012a, *ApJ*, 744, 23
- Zhang, B., Reid, M. J., Menten, K. M., Zheng, X. W., & Brunthaler, A. 2012b, *A&A*, 544A, 42

7. Online Material

7.1. Parallax and Proper Motion Fitting Details

Parallax fits are based on features persisting over 4 or more epochs. Internal maser motions are measured for features persisting over at least 3 epochs. Table 6 presents the results. The uncertainties of parallaxes and proper motions given in this table are the formal fitting uncertainties.

G074.03–01.71: We detected 13 features persisting over at least 3 epochs, only 3 of which lasted 6 epochs. These features mainly consist of three small groups located at (0,0), (0′1,–0′05) and (0′05,0′3), as shown in Fig. 23. The three features persisting over 6 epochs, used for the parallax fit, are located in the group at (0,0). We average the absolute proper motions of three groups as the source’s proper motion.

G075.76+00.33: There are 10 features persisting over at least 3 epochs, 6 of which lasted 6 epochs. All features are distributed in a ring and expand symmetrically relative the geometric center of the six persistent features (see Fig. 24). We average all the measured absolute proper motions as the source’s proper motion.

G075.78+00.34: We detect 20 features persisting over at least 3 epochs, 5 of which lasted 4 epochs. Fig 25 shows the proper motion relative to the center of the maser spots. We average all the measured absolute proper motions as the source’s proper motion.

G076.38–00.61: We detect three features persisting at least 3 epochs, belonging to two groups separated by about 80 mas in the NE-SW direction. A single feature lasted for 4 epochs and it is used for the parallax fit. The LSR velocities of the NE group are red shifted with respect to the SW group. The blue-shifted features to the SW expand with a very high velocity ($\sim 143 \text{ km s}^{-1}$) relative to the redshifted features, as shown in Fig. 26. We average the absolute proper motions of both groups as the source’s proper motion.

G079.87+01.17: We detected only 3 features persisting over at least 3 epochs, 1 of which lasted 6 epochs and it was used for the parallax fit. The amplitude of the internal proper motion is $\sim 10 \text{ km s}^{-1}$ (see Fig. 27). The absolute proper motion of the feature employed for the parallax fit is taken to be the source’s proper motion.

G090.21+02.32: We detected only 2 features persisting over at least 3 epochs, 1 of which lasted 6 epochs and it is used for the parallax fit. The other feature shows low relative velocity ($\sim 10 \text{ km s}^{-1}$), as shown in Fig. 28. The absolute proper motion of the feature employed for the parallax fit is taken to be the source’s proper motion.

G092.67+03.07: Although 27 features persisting over at least 3 epochs were detected,

only 2 of them persisted for 6 epochs and could be used for the parallax fit. The internal motions of these features are very complex (Fig. 29). We average all the measured absolute proper motions as the source’s proper motion.

G105.41+09.87: We detected only two features persisting for at least 3 epochs, one of which lasted for 5 epochs and was used for the parallax fit. The other feature had low relative velocity ($\sim 13 \text{ km s}^{-1}$), as shown in Fig. 30. We only used the feature employed for the parallax fit to derived the source’s proper motion.

Table 6:: Detailed Results of Parallax and Proper Motion measurements.

| Background Source | V_{LSR} (km s^{-1}) | Detected epochs | Parallax (mas) | μ_x (mas yr^{-1}) | μ_y (mas yr^{-1}) |
|------------------------|--|-----------------|-------------------|-------------------------------------|-------------------------------------|
| ON1 | | | | | |
| J2003+3034 | +14.8 | 111111 | 0.397 ± 0.045 | -3.53 ± 0.07 | -5.41 ± 0.04 |
| | +10.6 | 111111 | 0.421 ± 0.018 | -2.97 ± 0.02 | -5.60 ± 0.06 |
| | +10.6 | 011111 | 0.431 ± 0.036 | -3.16 ± 0.05 | -5.61 ± 0.07 |
| Combined fit | | | 0.425 ± 0.021 | | |
| Average | | | | -3.22 ± 0.05 | -5.54 ± 0.06 |
| G074.03–01.71 | | | | | |
| center group | | | | | |
| J2025+3343 | +12.5 | 111111 | 0.665 ± 0.010 | -3.59 ± 0.05 | -3.55 ± 0.07 |
| | +12.9 | 111111 | 0.602 ± 0.015 | -3.65 ± 0.05 | -3.76 ± 0.07 |
| | +13.4 | 111111 | 0.624 ± 0.012 | -3.48 ± 0.05 | -3.68 ± 0.07 |
| | +6.9 | 001110 | | -7.30 ± 0.48 | -4.20 ± 0.43 |
| Average | | | | -4.51 ± 0.16 | -3.80 ± 0.16 |
| Southeast group | | | | | |
| | +0.8 | 111110 | | -3.57 ± 0.09 | -5.58 ± 0.14 |
| | -1.1 | 111000 | | -6.04 ± 0.24 | -9.71 ± 0.33 |
| | +2.4 | 111110 | | -3.89 ± 0.07 | -6.45 ± 0.31 |
| | +4.3 | 011111 | | -2.72 ± 0.30 | -5.97 ± 0.20 |
| | +2.1 | 011100 | | -5.51 ± 0.05 | -6.27 ± 0.21 |
| | +1.6 | 001110 | | -6.33 ± 0.28 | -11.0 ± 1.87 |
| | +3.1 | 000111 | | -3.99 ± 0.45 | -5.74 ± 0.28 |
| Average | | | | -4.58 ± 0.21 | -7.25 ± 0.48 |
| Northwest group | | | | | |
| | +5.7 | 111000 | | -3.50 ± 0.15 | -3.39 ± 0.14 |

Table 6:: continued.

| Background Source | V_{LSR} (km s^{-1}) | Detected epochs | Parallax (mas) | μ_x (mas yr^{-1}) | μ_y (mas yr^{-1}) |
|----------------------|--|-----------------|-------------------|-------------------------------------|-------------------------------------|
| | +7.0 | 001110 | | -1.05 ± 0.16 | -3.77 ± 0.08 |
| Average | | | | -2.28 ± 0.16 | -3.58 ± 0.11 |
| Combined fit | | | 0.629 ± 0.010 | | |
| Average | | | | -3.79 ± 0.18 | -4.88 ± 0.25 |
| G075.76+00.33 | | | | | |
| J2015+3710 | -11.3 | 111111 | 0.285 ± 0.004 | -2.09 ± 0.01 | -4.76 ± 0.15 |
| | -10.9 | 011111 | | -2.05 ± 0.09 | -4.92 ± 0.04 |
| | -10.4 | 111111 | 0.299 ± 0.012 | -3.44 ± 0.04 | -4.43 ± 0.08 |
| | -9.6 | 111111 | 0.291 ± 0.017 | -3.34 ± 0.04 | -5.26 ± 0.08 |
| | -9.2 | 111111 | 0.307 ± 0.017 | -2.81 ± 0.04 | -4.05 ± 0.09 |
| | -8.8 | 111100 | | -3.84 ± 0.18 | -4.77 ± 0.09 |
| | -7.9 | 111101 | | -2.86 ± 0.05 | -4.04 ± 0.10 |
| | -7.1 | 111111 | 0.236 ± 0.033 | -4.42 ± 0.14 | -3.52 ± 0.06 |
| | -5.0 | 111111 | 0.268 ± 0.010 | -2.74 ± 0.03 | -4.09 ± 0.05 |
| | -4.6 | 111100 | | -3.22 ± 0.01 | -5.78 ± 0.10 |
| Combined fit | | | 0.285 ± 0.009 | | |
| Average | | | | -3.08 ± 0.06 | -4.56 ± 0.08 |
| G075.78+00.34 | | | | | |
| J2015+3710 | -8.4 | 1110 | | -5.10 ± 0.02 | -4.80 ± 0.05 |
| | -5.9 | 0111 | | -2.23 ± 0.04 | -3.94 ± 0.07 |
| | -3.8 | 1011 | | -2.94 ± 0.08 | -4.68 ± 0.08 |
| | -2.5 | 0111 | | -1.89 ± 0.03 | -5.48 ± 0.06 |
| | +0.0 | 1110 | | -2.87 ± 0.08 | -4.78 ± 0.07 |
| | +0.4 | 1111 | 0.258 ± 0.015 | -1.86 ± 0.02 | -5.13 ± 0.03 |
| | +0.4 | 1011 | | -1.77 ± 0.08 | -5.02 ± 0.14 |
| | +1.3 | 0111 | | -2.98 ± 0.13 | -5.53 ± 0.09 |
| | +1.7 | 1110 | | -3.37 ± 0.02 | -3.99 ± 0.03 |
| | +1.7 | 1110 | | -1.64 ± 0.19 | -4.79 ± 0.03 |
| | +2.1 | 0111 | | -1.98 ± 0.16 | -4.91 ± 0.17 |
| | +2.5 | 0111 | | -3.46 ± 0.05 | -4.23 ± 0.10 |
| | +2.5 | 1110 | | -1.61 ± 0.05 | -5.25 ± 0.06 |
| | +2.9 | 1111 | 0.301 ± 0.056 | -3.08 ± 0.06 | -4.94 ± 0.11 |

Table 6:: continued.

| Background Source | V_{LSR} (km s^{-1}) | Detected epochs | Parallax (mas) | μ_x (mas yr^{-1}) | μ_y (mas yr^{-1}) |
|----------------------------------|--|-----------------|-------------------|-------------------------------------|-------------------------------------|
| | +3.4 | 1111 | 0.310 ± 0.044 | -2.28 ± 0.05 | -4.43 ± 0.06 |
| | +3.4 | 0111 | | -3.23 ± 0.02 | -4.70 ± 0.01 |
| | +3.8 | 1111 | 0.270 ± 0.026 | -3.49 ± 0.03 | -2.87 ± 0.04 |
| | +4.2 | 1111 | 0.289 ± 0.019 | -2.91 ± 0.02 | -4.88 ± 0.02 |
| | +4.6 | 1110 | | -3.11 ± 0.03 | -4.99 ± 0.15 |
| | +9.3 | 1110 | | -3.92 ± 0.19 | -5.09 ± 0.04 |
| Combined fit | | | 0.281 ± 0.015 | | |
| Average | | | | -2.79 ± 0.07 | -4.72 ± 0.07 |
| G076.38–00.61 | | | | | |
| Northeast redshift group | | | | | |
| J2015+3710 | +6.9 | 111100 | 0.770 ± 0.053 | $+6.64 \pm 0.41$ | -0.11 ± 0.12 |
| Southwest blueshift group | | | | | |
| | –13.3 | 011100 | | -11.21 ± 0.88 | -6.34 ± 0.20 |
| | –13.3 | 011100 | | -16.98 ± 4.70 | -8.78 ± 1.23 |
| Average | | | | -14.10 ± 2.79 | -7.56 ± 0.72 |
| Combined fit | | | 0.770 ± 0.053 | | |
| Average | | | | -3.73 ± 1.60 | -3.84 ± 0.42 |
| G079.87+01.17 | | | | | |
| J2007+4029 | –4.6 | 1111110 | 0.620 ± 0.027 | -3.23 ± 0.07 | -5.19 ± 0.15 |
| G090.21+02.32 | | | | | |
| J2056+4940 | –6.2 | 111111 | 1.487 ± 0.064 | -0.66 ± 0.18 | -0.93 ± 1.11 |
| J2059+4851 | –6.2 | 111111 | 1.481 ± 0.081 | -0.68 ± 0.18 | -0.76 ± 1.11 |
| J2114+4953 | –6.2 | 111111 | 1.481 ± 0.079 | -0.68 ± 0.18 | -1.02 ± 1.11 |
| Combined fit | | | 1.483 ± 0.038 | -0.67 ± 0.10 | -0.90 ± 0.59 |
| G092.67+03.07 | | | | | |
| J2117+5431 | +0.1 | 111000 | | -2.12 ± 0.01 | -4.56 ± 0.28 |
| | –0.5 | 111000 | | $+2.46 \pm 2.26$ | -1.76 ± 0.84 |
| | –1.1 | 011110 | | -0.99 ± 0.31 | -2.67 ± 0.27 |
| | –1.8 | 111110 | | -2.44 ± 0.11 | -4.28 ± 0.11 |
| | –2.5 | 000111 | | -1.95 ± 0.22 | -3.29 ± 0.31 |

Table 6:: continued.

| Background Source | V_{LSR} (km s^{-1}) | Detected epochs | Parallax (mas) | μ_x (mas yr^{-1}) | μ_y (mas yr^{-1}) |
|----------------------|--|-----------------|-------------------|-------------------------------------|-------------------------------------|
| | -3.5 | 001110 | | -2.15 ± 0.35 | -2.76 ± 0.52 |
| | -3.7 | 111111 | 0.635 ± 0.010 | -1.70 ± 0.03 | -3.15 ± 0.08 |
| | -4.9 | 011111 | | -1.83 ± 0.16 | -4.68 ± 0.22 |
| | -6.2 | 011110 | | -1.74 ± 0.11 | -3.65 ± 0.26 |
| | -6.5 | 111100 | | -2.01 ± 0.07 | -4.57 ± 0.03 |
| | -6.8 | 001110 | | -2.70 ± 0.05 | -4.47 ± 0.44 |
| | -7.4 | 111100 | | -2.39 ± 0.14 | -4.41 ± 0.14 |
| | -8.3 | 111000 | | -1.18 ± 0.28 | -3.21 ± 0.38 |
| | -10.0 | 111000 | | -1.47 ± 0.01 | $+0.41 \pm 0.01$ |
| | -10.7 | 111000 | | -0.17 ± 0.12 | -2.69 ± 0.32 |
| | -12.8 | 111000 | | $+1.24 \pm 0.36$ | -2.25 ± 1.13 |
| | -13.7 | 001110 | | $+0.21 \pm 0.05$ | -5.12 ± 0.47 |
| | -14.3 | 011110 | | $+0.95 \pm 0.07$ | -1.07 ± 0.23 |
| | -14.3 | 111111 | 0.593 ± 0.023 | -0.03 ± 0.06 | -1.81 ± 0.25 |
| | -14.5 | 111000 | | $+1.47 \pm 0.01$ | -1.21 ± 0.12 |
| | -15.2 | 111000 | | $+0.90 \pm 0.51$ | -0.73 ± 0.09 |
| | -16.2 | 111110 | | $+0.82 \pm 0.30$ | -1.45 ± 0.64 |
| | -26.6 | 011110 | | -1.59 ± 0.27 | -1.85 ± 0.45 |
| | -29.5 | 111000 | | $+1.49 \pm 0.79$ | $+0.04 \pm 0.42$ |
| | -33.7 | 001011 | | -1.55 ± 0.12 | $+2.03 \pm 0.15$ |
| | -36.5 | 111000 | | $+0.41 \pm 0.21$ | $+0.68 \pm 0.71$ |
| | -37.4 | 001110 | | -0.55 ± 0.02 | $+1.82 \pm 0.06$ |
| Combined fit | | | 0.613 ± 0.014 | | |
| Average | | | | -0.69 ± 0.26 | -2.25 ± 0.33 |
| G105.41+09.87 | | | | | |
| J2203+6750 | -12.1 | 0011111 | 1.129 ± 0.063 | -0.21 ± 0.24 | -5.49 ± 0.13 |

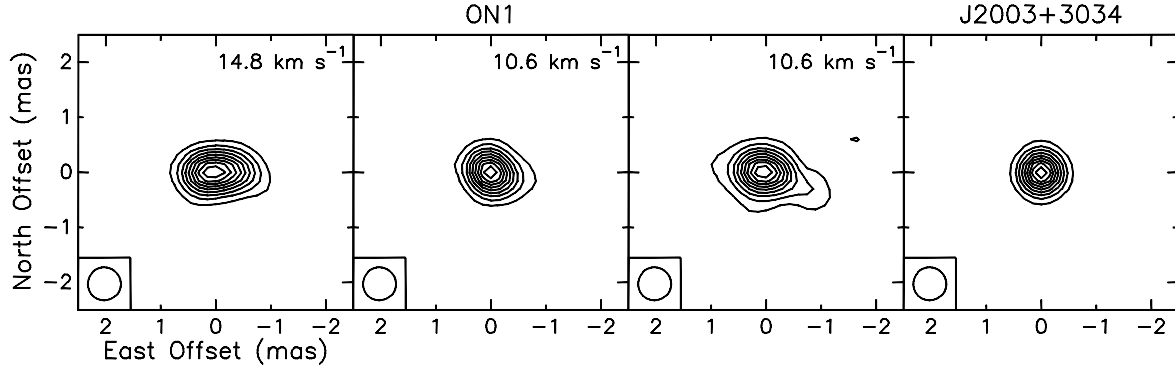


Fig. 14.— Maser channel-maps of ON 1 and the phase-reference source J2003+3034 for the second epoch (2009 May 7) (the spot at $V_{\text{LSR}} = 10.6 \text{ km s}^{-1}$ was not detected at the first epoch). The channel velocities and restoring beams are given in the upper right and lower left corner of each panel. Contour levels are integer multiples of 10% of the peak brightness of 34.1, 5.9 and 3.6 Jy beam^{-1} for ON 1 (from left to right) and 0.1 Jy beam^{-1} for J2003+3034. The two spots at $V_{\text{LSR}} = 10.6 \text{ km s}^{-1}$ have a separation of $\sim 35 \text{ mas}$. They appear to be compact and excellent astrometric targets.

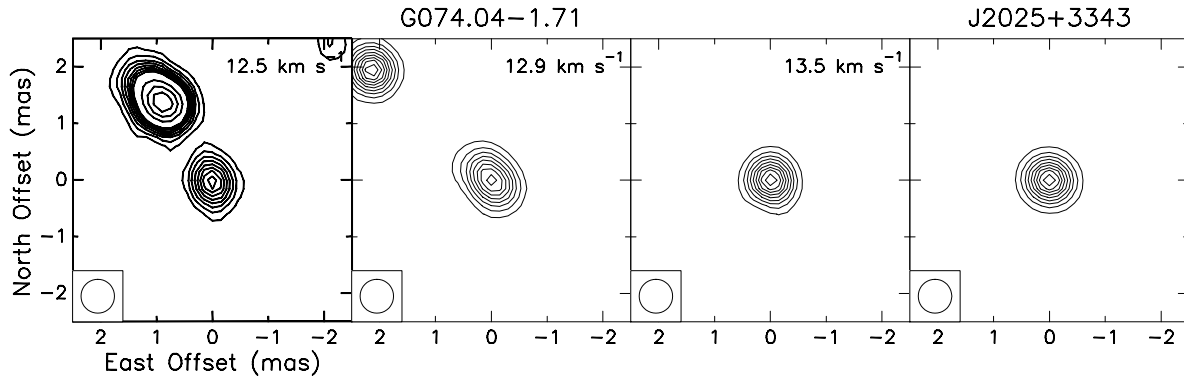


Fig. 15.— Maser channel-maps of G074.03-01.71 and the phase-reference source J2025+3343 for the first epoch (2010 April 24). Contour levels are integer multiples of 10% of the peak brightness of 0.3, 0.5 and 0.6 Jy beam^{-1} for G074.03-01.71 (from left to right) and 3.9 Jy beam^{-1} for J2025+3343. The maser spots at the center of the images are used for the parallax fit.

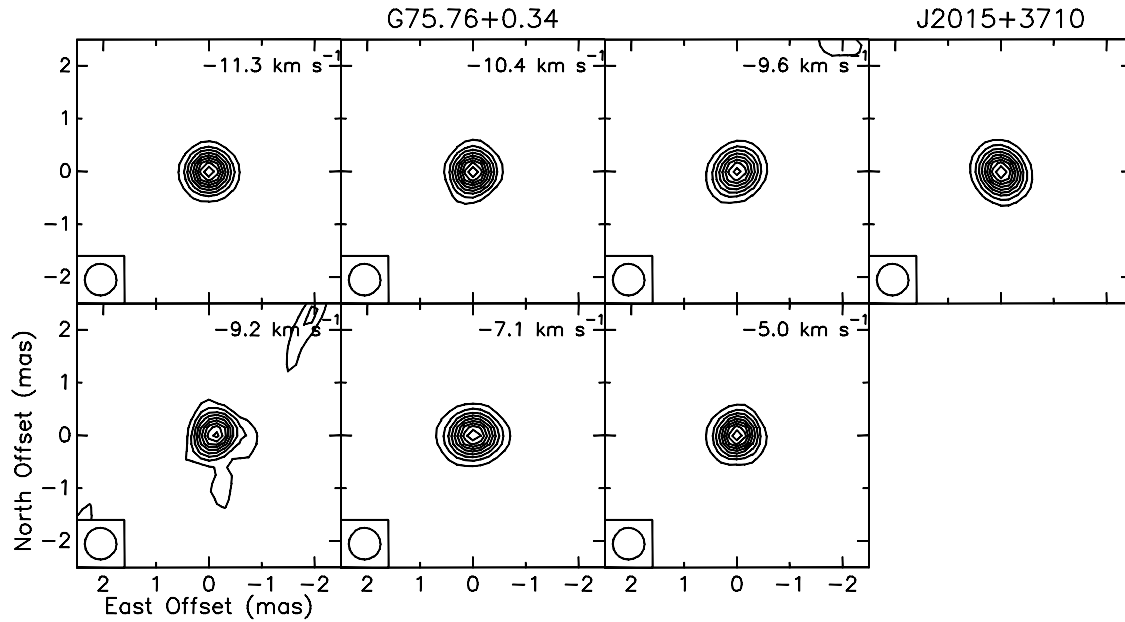


Fig. 16.— Maser channel-maps of G075.76+0.33 and the phase-reference source J2015+3710 for the first epoch (2010 April 24). Contour levels are integer multiples of 10% of the peak brightness of 3.3, 2.4, 5.3, 0.5, 1.4 and 0.7 Jy beam^{-1} for G075.76+0.33 (from upper left to lower right) and 3.9 Jy beam^{-1} for J2015+3710.

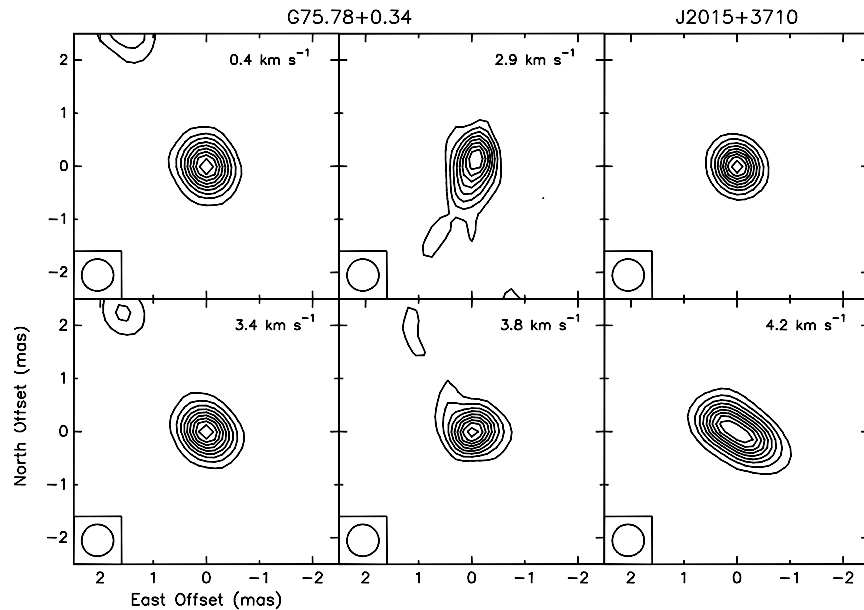


Fig. 17.— Maser channel-maps of G075.78+0.34 and the phase-reference source J2015+3710 for the first epoch (2009 May 7). Contour levels are integer multiples of 10% of the peak brightness of 26.7, 2.4, 58.8, 6.0 and 10.8 Jy beam^{-1} for G075.78+0.34 (from upper left to lower right) and 2.3 Jy beam^{-1} for J2015+3710.

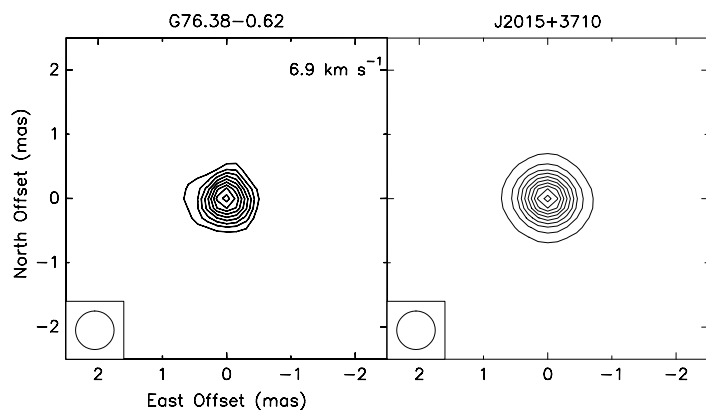


Fig. 18.— Maser channel-map at $V_{\text{LSR}} = 6.9 \text{ km s}^{-1}$ of G076.38–00.61 and the phase-reference source J2015+3710 for the first epoch (2010 April 24). Contour levels are integer multiples of 10% of the peak brightness of 0.2 Jy beam^{-1} for G076.38–00.61 and 1.6 Jy beam^{-1} for J2015+3710.

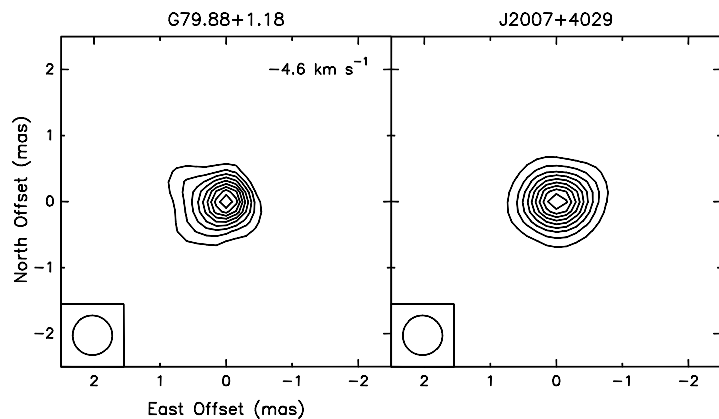


Fig. 19.— Maser channel-map at $V_{\text{LSR}} = -4.6 \text{ km s}^{-1}$ of G079.87+01.17 and the phase-reference source J2007+4029 for the first epoch (2011 May 24). Contour levels are integer multiples of 10% of the peak brightness of 8.0 for G079.87+01.17, and 1.6 Jy beam^{-1} J2007+4029, respectively.

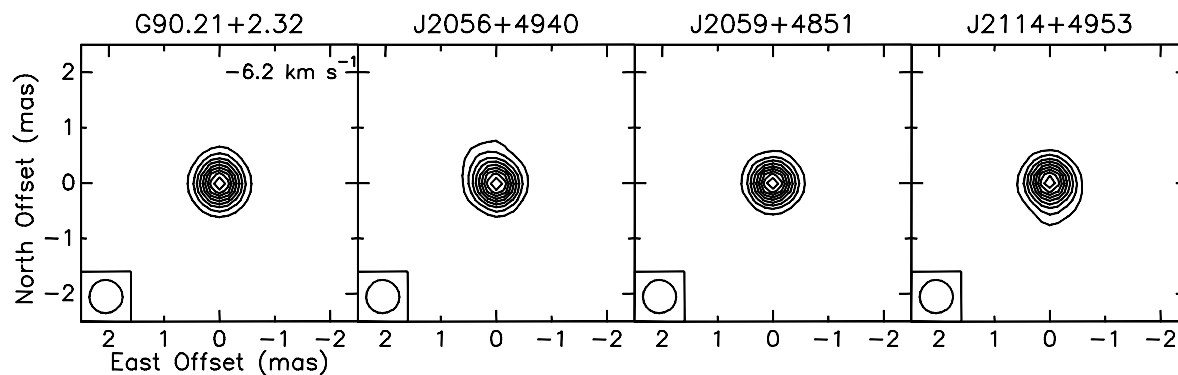


Fig. 20.— Image of the maser channel at $V_{\text{LSR}} = -6.2 \text{ km s}^{-1}$ of G090.21+02.32 and the background sources J2056+4940, J2059+4851 and J2114+4953 for the first epoch (2010 May 16). Contour levels are at integer multiples of 10% of the peak brightness of $17.0 \text{ Jy beam}^{-1}$ for G090.21+02.32 and 0.03 , 0.05 and $0.06 \text{ Jy beam}^{-1}$ for J2056+4940, J2059+4851 and J2114+4953, respectively.

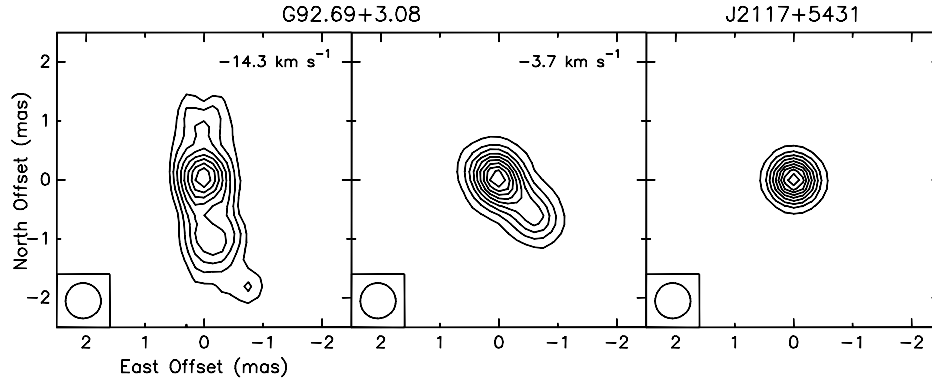


Fig. 21.— Maser channel-maps of G92.67+03.07 and the phase-reference source J2117+5431 for the first epoch (2010 May 16). Contour levels are integer multiples of 10% of the peak brightness of 26.1 and $16.4 \text{ Jy beam}^{-1}$ (from left to right) for G92.67+03.07 and 0.2 Jy beam^{-1} for J2117+5431.

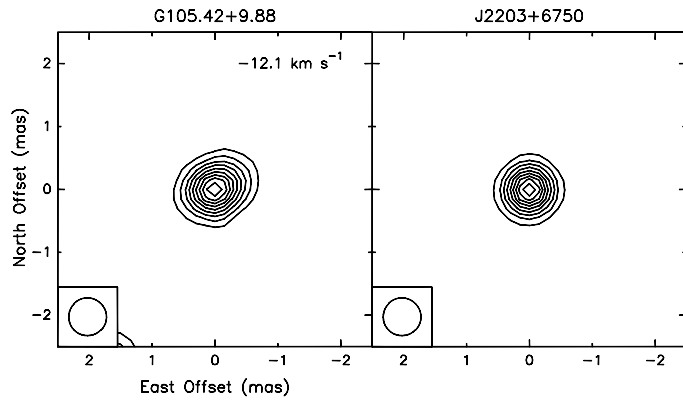


Fig. 22.— Maser channel-map at $V_{\text{LSR}} = -12.1 \text{ km s}^{-1}$ of G105.41+09.87 and the phase-reference source J2203+6750 for the third epoch (2011 October 30). Contour levels are integer multiples of 10% of the peak brightness of 2.2 Jy beam^{-1} for G105.41+09.87 and 0.2 Jy beam^{-1} for J2203+6750, respectively.

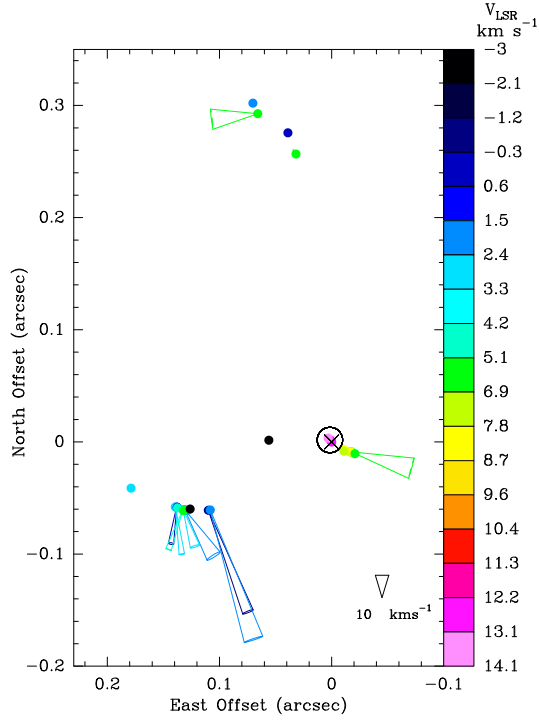


Fig. 23.— Distributions of H₂O masers in G074.03–01.71. Maser LSR velocities are indicated by the color scale on the righthand side of the plot. The cones indicate the 3-D velocities relative to the persistent spot (marked with a cross) at $V_{\text{LSR}} = 13.4 \text{ km s}^{-1}$: R.A.(J2000) = $20^{\text{h}}25^{\text{m}}07.1053^{\text{s}}$ and Dec.(J2000) = $34^{\circ}49'57.593''$ on 2010 April 24. The cone opening angle gives the 1σ uncertainty on the proper motion direction. The length of the cone is proportional to the velocity, with a 10 km s^{-1} scale indicated in the lower right corner. Points without associated cones were detected in fewer than three epochs. The maser features used for the determination of the parallax are marked with black circles.

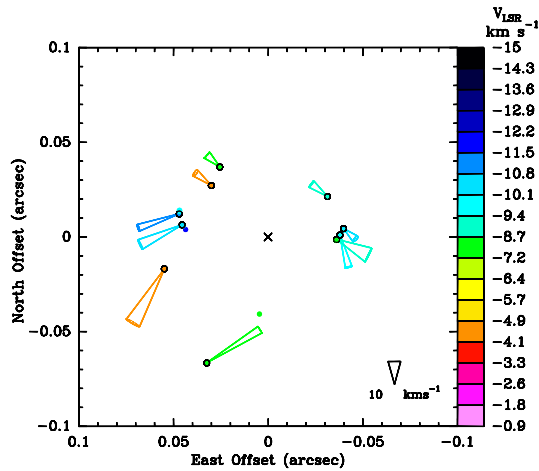


Fig. 24.— Distributions of H₂O masers in G075.76+00.33. Symbols and cones have the same meaning as in Fig. 23, except that the proper motions are relative to the the geometric center (x) of the features persisting over the 6 observing epochs: R.A.(J2000) = $20^{\text{h}}21^{\text{m}}41.0894^{\text{s}}$ and Dec.(J2000) = $37^{\circ}25'29.274''$ on 2010 April 24. The maser features used for the determination of the parallax and source’s proper motion are marked with black circles.

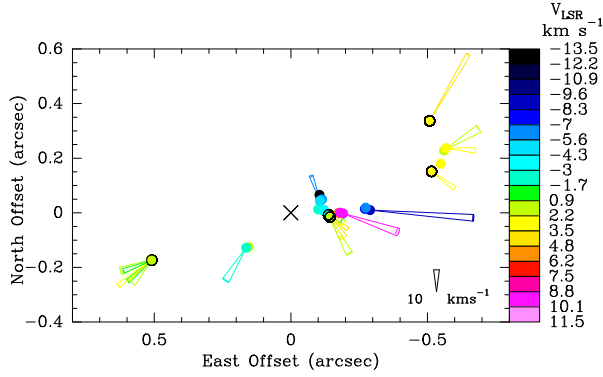


Fig. 25.— Distributions of H_2O masers in G075.78+00.34. Symbols and cones have the same meaning as in Fig. 23, except that the proper motions are relative to the geometric center (x) of the features persisting over the 4 observing epochs: R.A.(J2000) = $20^{\text{h}}21^{\text{m}}44.0218^{\text{s}}$ and Dec.(J2000) = $37^{\circ}26'37.462''$ on 2009 May 7. The maser features used for the determination of the parallax are marked with black circles.

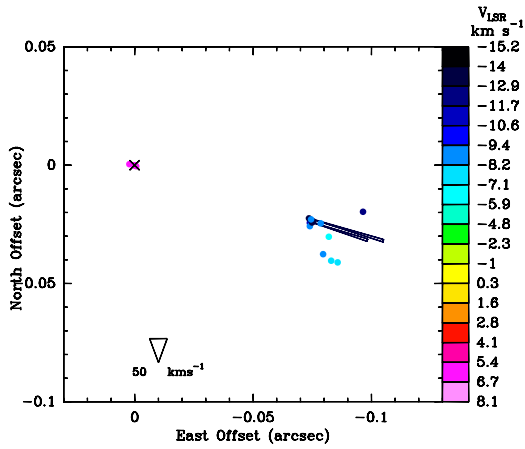


Fig. 26.— Distributions of H_2O masers in G076.38–00.61. Symbols and cones have the same meaning as in Fig. 23. The proper motions are relative to the persistent spot used for the parallax fit (marked with a cross) at $V_{\text{LSR}} = 6.9 \text{ km s}^{-1}$: R.A.(J2000) = $20^{\text{h}}27^{\text{m}}25.4816^{\text{s}}$ and Dec.(J2000) = $37^{\circ}22'48.482''$ on 2010 April 24.

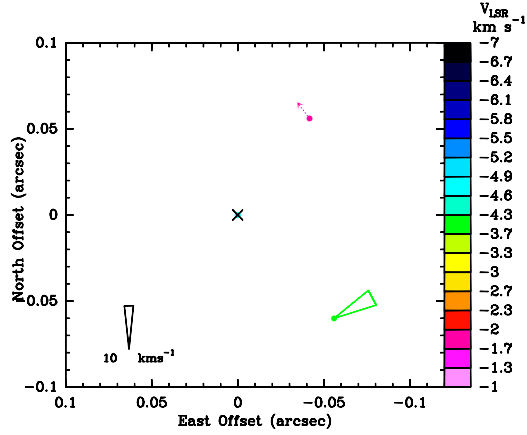


Fig. 27.— Distributions of H₂O masers in G079.87+01.17. Symbols and cones have the same meaning as in Fig. 23. The proper motions are relative to the persistent spot used for the parallax fit (marked with a cross) at $V_{\text{LSR}} = -4.6 \text{ km s}^{-1}$: R.A.(J2000) = 20^h30^m29.1464^s and Dec.(J2000) = 41°15′53.590″ on 2011 May 24.

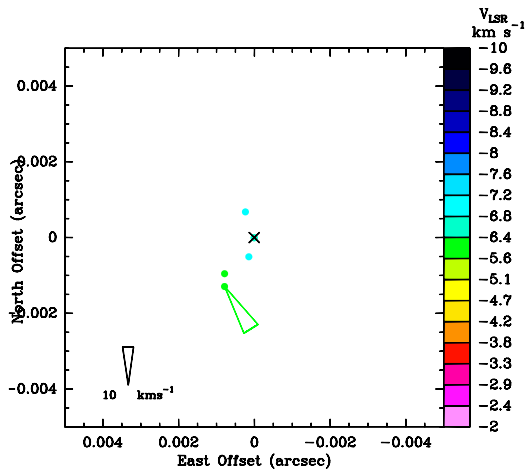


Fig. 28.— Distributions of H₂O masers in G090.21+02.32. Symbols and cones have the same meaning as in Fig. 23. The proper motions are relative to the persistent spot used for the parallax fit (marked with a cross) at $V_{\text{LSR}} = -6.2 \text{ km s}^{-1}$: R.A.(J2000) = 21^h02^m22.7007^s and Dec.(J2000) = 50°03′08.309″ on 2010 May 16.

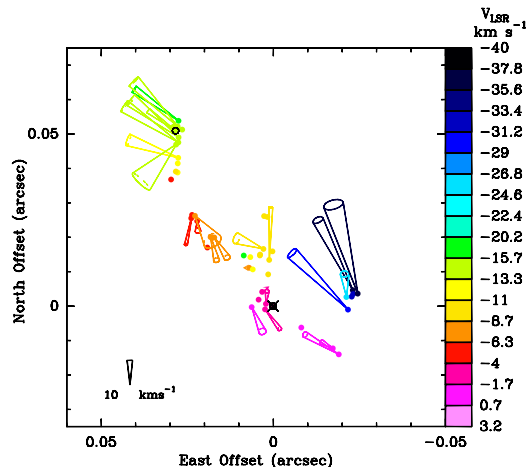


Fig. 29.— Distributions of H_2O masers in G092.67+03.07. Symbols and cones have the same meaning as in Fig. 23. The proper motions are relative to the persistent spot (marked with a cross) at $V_{\text{LSR}} = -3.7 \text{ km s}^{-1}$; R.A.(J2000) = $21^{\text{h}}09^{\text{m}}21.7232^{\text{s}}$ and Dec.(J2000) = $52^{\circ}22'37.083''$ on 2010 May 16. The maser features used for the determination of the parallax are marked with black circles.

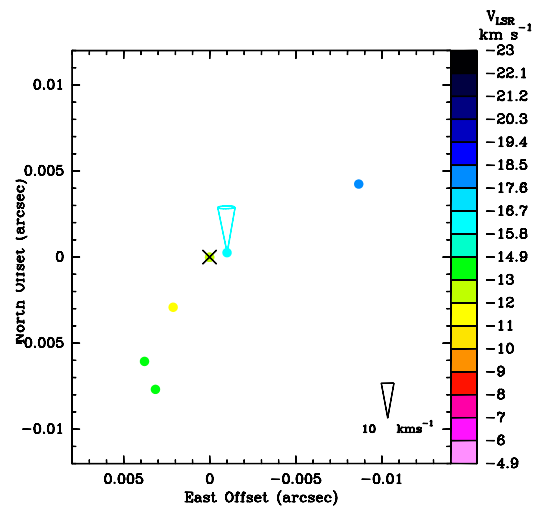


Fig. 30.— Distributions of H_2O masers in G105.41+09.87. Symbols and cones have the same meaning as in Fig. 23. The proper motions are relative to the persistent spot used for the parallax fit (marked with a cross) at $V_{\text{LSR}} = -12.1 \text{ km s}^{-1}$; R.A.(J2000) = $21^{\text{h}}43^{\text{m}}06.4628^{\text{s}}$ and Dec.(J2000) = $66^{\circ}06'55.183''$ on 2011 October 30.